Available online at www.sciencedirect.com
ScienceDirect
Geochimica et Cosmochimica Acta 71 (2007) 1249–1265
Geochimica
www.elsevier.com/locate/gca

A computer simulation study of natural silicate melts. Part I: Low pressure properties

Bertrand Guillot *, Nicolas Sator

Laboratoire de Physique Théorique de la Matière Condensée, Université Pierre et Marie Curie (Paris 6), UMR CNRS 7600, 4 place Jussieu, 75252 Paris Cedex 05, France

Received 31 March 2006; accepted in revised form 13 November 2006

Abstract

In implementing into a molecular dynamics simulation code a simple interionic potential developed to describe the nine component system K_2O–Na_2O–CaO–MgO–FeO–Fe_2O_3–Al_2O_3–TiO_2–SiO_2 (KNCMFATS), it has been possible to reproduce satisfactorily a number of thermodynamic, structural and transport properties of a representative set of natural silicate melts. An important conclusion reached in this study is the good transferability of the potential from felsic to ultramafic compositions although this transferability becomes less accurate with high silica contents (rhyolitic composition and beyond) and with very iron-rich silicates (e.g. fayalite). A key feature of the simulation is to make the link between macroscopic properties of the melt and its microscopic structure and dynamics. We thus obtain a relationship between the molar volume of the melt, the number of network modifiers and the oxygen coordination number. The simulation also allows one to quantify the coordination environment around the cations as function of the melt composition. Furthermore, the electrical conductivity of the high temperature liquid is investigated.

1. Introduction

Magmatism plays or played a fundamental role on Earth and on other terrestrial planets. The production rate of oceanic crust at mid-oceanic ridges amounts to 20 km^3/yr (Perfit and Davidson, 2000) along the 75,000 km plate boundaries and, since the early Archean about 20% (vol) of the upper mantle has been melted and involved in the formation of oceanic crust. This is likely a conservative estimate since the mantle was significantly hotter in the Archean than nowadays. There are some indications that the Earth was extensively molten at the end of the accretion period (Tonks and Melosh, 1993), this magma ocean crystallizing progressively from the lower mantle to the upper mantle leading to a chemical differentiation and to the constitution of a protocrust (Caro et al., 2005). Recently it has been advocated that giant impactors can cause volcanism (Elkins-Tanton and Hager, 2005) and melt widespread area creating flood basalt similar to that observed in large igneous provinces.

These examples of magmatism illustrate the point that a clear understanding of the mechanisms at work in the Earth's mantle requires a better knowledge of the thermodynamic, structural, and transport properties of natural silicate melts. However, the variation in the composition of natural silicates, made up of the nine most abundant oxides (SiO_2, TiO_2, Al_2O_3, Fe_2O_3, FeO, MgO, CaO, Na_2O, and K_2O) is large and covers a quasi continuum range between felsic to ultramafic composition. For this reason it is virtually impossible to measure properties of all these compositions in a large pressure–temperature domain. Hence there were several attempts to propose an analytical scheme to predict the density (Bockris et al., 1956; Bottinga and Weill, 1970; Bottinga et al., 1982, 1983; Lange and Carmichael, 1987; Knoche et al., 1995; Lange, 1997; Ghiorso, 2004; Ghiorso and Kress, 2004), the heat capacity (Stebbins et al., 1984) and the viscosity (Russel and Giordano, 2005) for any composition of the melt.

* Corresponding author. Fax: +33 1 44 27 51 00.
E-mail address: guillot@lptl.jussieu.fr (B. Guillot).

0016-7037/$ - see front matter © 2006 Elsevier Inc. All rights reserved.
doi:10.1016/j.gca.2006.11.015

An alternative route, that we will follow here, is to use computer modeling to evaluate the properties of natural silicate melts. Among the existing molecular simulation methods (Allen and Tildesley, 1987; Frenkel and Smit, 1996), the molecular dynamics method (MD) is particularly convenient since it permits one to calculate thermodynamic, structural and transport properties of a liquid sample composed of thousands of atoms. The core of the calculation consists of solving the Newton equations of motion associated with an assembly of particles (e.g. ions) interacting through a given force field, the latter one being determined either empirically or from first principles (ab initio calculation). In the case of the empirical force fields dedicated to crystalline and molten silicates, the charge distribution on each atom is represented by a point charge whose magnitude is identified with the formal charge of the ion in the corresponding oxide (e.g. for SiO_2: $q_{Si} = +4e$, $q_O = -2e$), while the exchange repulsion energy between the atoms is accounted for by a Born–Huggins–Mayer exponential term supplemented (or not) by dispersion forces ($E_{disp} \sim C/r^6$). After the pioneering work on silica by Woodcock et al. (1976), a number of MD studies based on this simple interaction model have been published for molten binary and ternary silicates (Soules, 1979; Angell et al., 1983; Kubicki and Lasaga, 1988, 1991; Kieffer and Angell, 1989; Stein and Spera, 1995, 1996; Belashchenko, 1996; Morgan and Spera, 2001). In order to improve the simulated network topology with respect to structure data, three-body terms mimicking covalent interactions were introduced to constrain O–T–O and T–O–T bond angle distribution, where T is a structure former ion (e.g. Feuston and Garofalini, 1988; Vessal et al., 1989; Vashishta et al., 1990). Since then, molten silicates of increasing complexity, involving up to five different oxides have been investigated by MD simulations with these improved potentials (e.g. Huang and Cormack, 1990; Smith et al., 1995; Delaye et al., 1997, 2001; Rossano et al., 2000a; Ganster et al., 2004). However, an important progress was the recognition that in the crystalline state, the electronic redistribution between ions induced by short and long range interactions could be reproduced by using effective charges instead of formal charges (Tsuneyuki et al., 1988; van Beest et al., 1990; Tangney and Scandolo, 2002). This simple ansatz allows to evaluate with a good accuracy the elastic constants of the crystalline polymorphs of silica (Tsuneyuki et al., 1990; Herzbach et al., 2005), or to investigate the behavior of liquid silica under pressure (Rustad et al., 1990; Tangney and Scandolo, 2002), for instance. We report here the results of MD calculations based upon a new empirical interaction potential and dedicated to molten silicates where the variation in composition covers most of the natural silicates involved in magmatic processes. Our methodology as well as computational details are given in Section 2, while the thermodynamics, the structure and transport properties of the simulated melts are reported in Section 3 and are compared with existing experimental data. The main conclusions drawn from this study are summarized in Section 4.

2. Methodology and computational details

Our objective is to investigate by classical MD simulation the thermodynamics, the structure and the transport properties of a large variety of natural silicate melts. For this purpose we have developed a simple force field to describe silicate melts made up of the nine geologically most abundant oxide components (SiO_2, TiO_2, Al_2O_3, FeO, Fe_2O_3, MgO, CaO, Na_2O, and K_2O). This interatomic potential is computationally inexpensive to perform long simulation runs for adequate system sizes, highly transferable with composition and sufficiently accurate to reproduce the variability of behavior observed in real magmatic liquids.

As emphasized in the introduction, simple ionic potentials using effective partial charges are able to reproduce satisfactorily the crystalline polymorphs of silica (Tsuneyuki et al., 1990; van Beest et al., 1990). Furthermore, an ab initio molecular dynamics simulation of vitreous silica has shown (Benoit et al., 2000) that the energetic basin explored by the electronic structure calculation is very similar to that described by the ionic potential of van Beest et al. (1990). This result supports the idea that the reorganization of the electronic density throughout the melt, via charge transfer and polarization effects, can be modeled in an effective way by assigning partial charges to the ions. So it is noteworthy that Matsui (1994, 1996) has proposed an empirical potential using effective charges to describe the four component system CMAS (CaO, MgO, Al_2O_3, and SiO_2) and which reproduces satisfactorily, when implemented in a MD code, the structure, the molar volume and the bulk modulus of 27 crystals and four liquids belonging to this system. Later on this study was extended to the NCMAS system (Matsui, 1998).

Following the same philosophy, we will describe the interaction energy between atoms of a melt belonging to the KNCMFATS system by a sum of pairwise interactions namely,

$$v(r_{ij}) = z_i z_j / r_{ij} + B_{ij} e^{-r_{ij}/\rho_{ij}} - C_{ij}/r_{ij}^6 \quad (1)$$

where r_{ij} is the distance between atoms i and j, z_i is the effective charge associated with the atom i, and where B_{ij}, ρ_{ij} and C_{ij} are energy parameters for the pair ij describing repulsive and dispersive forces, respectively. To ensure the transferability of the interaction potential with the composition of the melt, the electroneutrality of the individual oxide components is assumed, i.e. the valence of the oxygen is kept fixed (when determined) irrespective of its environment (other choices are possible, see Demilrap et al., 1999). The contribution of the dispersion energy ($-C/r^6$) is small with respect to charge–charge, charge-transfer and induction energy and an accurate determination by ab initio calculations is a difficult task. Moreover, when short interatomic distances are sampled during a MD simulation, it may happen occasionally (for some values of the potential parameters and when investigating

a liquid at high temperature) that the dispersion term leads to an unphysical singularity catastrophe, thereby overwhelming all the others in the potential energy. In this case the $1/r^6$ term has to be amended by an ad hoc damping function. Therefore, care must be taken when using it.

The potential parameters (z_i, B_{ij}, ρ_{ij} and C_{ij}) figuring in Eq. (1) have been determined by constraining the MD simulations to reproduce at best the density at zero pressure and the structure of a selected set of 11 natural silicate melts covering a large range of composition (from felsic to ultramafic). The description of these silicates is presented in the appendix and their composition is given in Table 1. The calculated density for a particular melt was compared either with experimental data when available or with the value obtained from empirical relations describing the volumetric properties of multicomponent silicate liquids (Bottinga and Weill, 1970; Bottinga et al., 1982, 1983; Lange and Carmichael, 1987; Lange, 1997; Ghiorso, 2004; Ghiorso and Kress, 2004).

To reduce the number of adjustable parameters in the potential, we assume that cation–cation interactions are governed only by electrostatics (charge–charge repulsion). This is a reasonable assumption for silicates where cation–oxygen and oxygen–oxygen interactions dominate at short range. Furthermore, the requirement of transferability imposes that,

$$z_{Si} = z_{Ti} = (4/3)z_{Al} = (4/3)z_{Fe^{3+}} = 2z_{Fe^{2+}} = 2z_{Mg} = 2z_{Ca} = 4z_{Na} = 4z_{K} = -2z_{O}, \quad (2)$$

which means that only the effective charge on the oxygen atom has to be determined. However, several sets of potential parameters are able to reproduce satisfactorily (at least for one given state point) the structure and the density of most of the investigated silicate melts. More precisely, our method does not lead to a unique value for the effective charge of oxygen but instead indicates a range of preferential values ($-1.2e < z_O < -0.8e$). In order to retain the good description of crystals in the CMAS system obtained by Matsui (1996) with his force field, we have used the same effective charge for oxygen ($z_O = -0.945e$) and optimized the other potential parameters to describe the KNCMFATS system. Our final parameter set is given in Table 2 while a comparison between simulation results and experimental data for various thermodynamic properties and structural data is presented in Tables 3 and 4, respectively. Although the latter results will be commented on in the next

Table 1
Chemical compositions (weight fraction) of the silicate melts investigated in this study

Silicate	SiO_2 (wt%)	TiO_2 (wt%)	Al_2O_3 (wt%)	Fe_2O_3 (wt%)	FeO (wt%)	MgO (wt%)	CaO (wt%)	Na_2O (wt%)	K_2O (wt%)	Total
Rhyolite (Ry)	74.51 (257)	0.10 (0)	13.25 (54)	0.32 (1)	1.28 (3)	0.08 (0)	0.75 (3)	4.15 (28)	5.64 (25)	100.08 (1000)
Andesite (And)	56.65 (203)	1.01 (3)	17.41 (73)	4.63 (12)	3.53 (11)	4.30 (23)	7.38 (28)	3.23 (22)	1.56 (7)	99.70 (998)
Basalt(MORB)	50.59 (185)	1.52 (4)	15.11 (65)	1.15 (3)	8.39 (26)	7.77 (42)	11.87 (47)	2.94 (21)	0.13 (1)	99.47 (1000)
Mars basalt (BM)	47.68 (176)	0.54 (1)	10.96 (48)	3.09 (9)	15.82 (49)	12.62 (69)	7.96 (31)	2.68 (19)	0.06 (0)	101.41 (1000)
Green glass (LG15)	48.00 (179)	0.26 (1)	7.74 (34)		16.50 (52)	18.20 (101)	8.57 (34)			99.27 (999)
Black glass (LG14)	34.00 (136)	16.40 (50)	4.60 (22)		24.50 (83)	13.30 (79)	6.90 (30)	0.23 (2)	0.16 (0)	100.09 (1000)
Komatiite (Ko)	46.73 (168)	0.31 (1)	6.30 (27)		10.76 (32)	28.42 (152)	6.29 (24)	0.85 (6)	0.13 (1)	99.79 (1001)
Peridotite (Pe)	45.10 (159)		2.80 (12)		10.40 (31)	38.40 (203)	3.40 (13)			100.10 (1001)
Olivine (Ol)	40.68 (142)		0.01 (0)		8.76 (25)	50.52 (262)	0.06 (0)			100.03 (1000)
Allende m. (All)	38.57 (147)	0.14 (0)	3.71 (17)		24.79 (79)	29.23 (166)	2.62 (11)	0.48 (3)		99.54 (1000)
Fayalite (Fa)	29.49 (143)				70.51 (286)					100.00 (1001)

Data sources are given in Appendix. In parenthesis are the numbers of cations of each species used in the simulation of the corresponding silicate melt. In the last column are indicated the total weight fraction and in parenthesis the total number of atoms (cations + oxygens) used in the simulation.

Table 2
Potential parameters

	z (e)	B (kJ/mol)	ρ (A)	C (A^6 kJ/mol)
O	−0.945 (−1.20)	870570.0 (889916.0)	0.265 (0.265)	8210.17 (8210.17)
Si	1.89 (2.40)	4853815.5 (5900530.0)	0.161 (0.161)	4467.07 (4467.07)
Ti	1.89	4836495.0	0.178	4467.07
Al	1.4175	2753544.3	0.172	3336.26
Fe^{3+}	1.4175	773840.0	0.190	0.0
Fe^{2+}	0.945 (1.20)	1257488.6 (1450950.0)	0.190 (0.190)	0.0 (0.0)
Mg	0.945	3150507.4	0.178	2632.22
Ca	0.945	15019679.1	0.178	4077.45
Na	0.4725	11607587.5	0.170	0.0
K	0.4725	220447.4	0.290	0.0

Values of B, ρ and C given in column 3, 4, and 5, respectively, correspond to cation–oxygen and oxygen–oxygen interactions, the cation–cation interactions being described only by coulombic repulsive forces. Values given in parenthesis for O, Si, and Fe^{2+} are solely for fayalite (see text).

Table 3
Thermodynamic properties of molten silicates around zero pressure

Silicate	ρ^g (g/cm^3)	ρ^l (g/cm^3)	α_P^g (10^{-5} K^{-1})	α_P^l (10^{-5} K^{-1})	C_P^l (J/mol K)
Rhyolite					
This work	2.45	2.31	3.6	7.1	111.5
Lit. data		2.36[a];2.29[b];2.29[c]		10.1[a]; 5.3[b]; 3.8[c]	88.6[i]; 87.3[j]
Andesite					
This work	2.83	2.58	3.2	9.8	110.0
Lit. data		2.52[d];2.51[b];2.51[c]		8.1[d];6.0[b];5.5[c]	95.8[i] ; 96.9[j]
MORB					
This work	2.95	2.65	4.7	11.1	102.5
Lit. data		2.65[e];2.63[b];2.63[c]		10.6[e];7.0[b];6.4[c]	93.8[i]
Mars					
This work	3.13	2.72	5.7	12.3	98.2
Lit. data		2.74[f];2.70[b];2.71[c]		7.1[f];7.7[b];7.4[c]	92.9[i]
LG15					
This work	3.18	2.79	4.4	12.2	94.0
Lit. data		2.79[b];2.81[c]		8.2[b];7.1[c]	90.2[i]
LG14					
This work	3.41	2.99	4.6	14.3	94.8
Lit. data		3.02[b];3.04[c]		11.8[b];11.8[c]	91.3[i]
Komatiite					
This work	3.09	2.73	4.6	13.1	90.8
Lit. data		2.69[g];2.74[b];2.77[c]		4.7[g];9.7[b];8.1[c]	91.5[i]
Peridotite					
This work	3.20	2.78	5.0	13.8	85.3
Lit. data		2.75[g];2.77[b];2.82[c]		6.4[g];11.0[b];8.9[c]	91.3[i]
Allende					
This work	3.34	2.86	6.0	14.6	85.7
Lit. data		2.98[b];3.02[c]		10.4[b];9.7[c]	89.8[i]
Olivine					
This work	3.20	2.78	4.8	14.3	82.0
Lit. data		2.82[b]; 2.88[c]		12.9[b];10.5[c]	92.0[i]
Fayalite					
This work	4.14	3.66	4.6	12.8	78.0
Lit. data		3.66[h];3.70[b];3.71[c]		9.0[h];7.5[b];10.6[c]	79.3[i]

ρ^g is the density of the glass at 400 K, ρ^l is the density of the liquid at 1800 K, α_P^g is the thermal expansion coefficient of the glass at 400 K, α_P^l is the thermal expansion coefficient of the liquid at 1800 K, C_P^l is the heat capacity of the high temperature liquid (above 2000 K when C_P^l becomes nearly constant). Values marked with superscripts are literature data (references are given at the end of the Table). Values for the glass at 400 K are only given for information since they depend on the cooling rate and the system size used in the simulation (e.g. q = 2.10^{11}K/s and $N \sim 1000$).

[a] For a synthetic rhyolite, see sample 12 in Nelson and Carmichael (1979).
[b] Evaluated from Ghiorso (2004).
[c] Evaluated from Lange and Carmichael (1987).
[d] For a synthetic iron-free andesite, see sample 2 in Nelson and Carmichael (1979). The value of the density was corrected for difference in molar mass due to the presence of iron in the simulated andesite (Unzen).
[e] For Kilauea basalt, see sample Kil 2 in Nelson and Carmichael (1979).
[f] For an iron-rich basaltic composition, see sample 005 in Mo et al. (1982).
[g] Courtial et al. (1997).
[h] Using a linear interpolation at 1800 K between data of Shiraishi et al. (1978) and that of Courtial et al. (1997).
[i] Evaluated from the heat capacity model of Stebbins et al. (1984).
[j] Values of C_P^l in Neuville et al. (1993) were taken at 1800 K for convenience.

section, it is noteworthy that the accuracy of the force field we use to evaluate the density of the magmatic liquids is generally better than 3% at 1800 K. For fayalite, the potential parameter set leads to a large underestimation of the density in the liquid range (by ~15% at 1800 K, not shown). This result can be understood if one takes into account the peculiarities of the FeO–SiO_2 system. Indeed, liquid FeO exhibits no ionic conduction whereas the addition of 30 mol% SiO_2, which is close to the fayalite composition, leads to a nearly complete ionic dissociation (Shiraishi et al., 1978). As opposed to silicates with lower Fe contents, our ionic field cannot suitably describe the fayalite composition, since the ionicity varies drastically with composition in the FeO–SiO_2 system. Thus fayalite suggests a limit to the transferability of our force field with composition. Nevertheless, a further scrutiny shows that fayalite can be conveniently described in determining a specific set of potential parameters (see in Table 2). Only the results for fayalite obtained with this latter parameter set are discussed in the following.

The MD calculations were performed with the code DL_POLY of the CCLRC library (Daresbury, UK). The equations of motion were integrated with the Verlet leap-frog algorithm (time step of 1 femtosecond) in using

Table 4
Structure of the liquid silicates at 2273 K

Silicate R_{xo}:N_{xo}/$R_{xx}N_{xx}$	Si	Ti	Al	Fe^{3+}	Fe^{2+}	Mg	Ca	Na	K	O
Rhyolite	1.63:4.0		1.74:4.0	1.83:4.0	2.07:4.8		2.39:7.0	2.46:7.6	3.18:7.5	2.66:7.0
	3.16:3.3		3.21:1.1							
Andesite	1.63:4.0	1.93:5.2	1.74:4.1	1.84:4.2	2.07:5.2	2.00:5.0	2.39:7.4	2.50:8.0	3.12:9.6	2.66:8.0
	3.14:2.8		3.20:1.4	3.43:0.2	3.40:0.2	3.20:0.5	3.84:1.0			
MORB	1.63:4.0	1.93:5.2	1.74:4.1	1.82:4.2	2.07:5.0	2.00:4.9	2.38:7.4	2.45:8.0	3.18:10.8	2.66:9.3
	3.16:2.2		3.16:1.2		3.44:0.4	3.18:1.1	3.88:1.5	2.94:1.0		
Mars	1.63:4.0	1.93:5.3	1.74:4.1	1.84:4.3	2.07:5.2	1.98:4.9	2.38:6.8	2.48:7.5		2.68:9.6
	3.16:2.0		3.20:1.0	3.45:0.2	3.54:1.5	3.14:1.8	3.71:1.1	2.94:0.9		
LG15	1.63:4.0	1.93:5.7	1.74:4.1		2.07:5.2	2.00:5.1	2.40:7.0			2.67:10.2
	3.16:2.2		3.22:0.6		3.43:1.7	3.18:2.8	3.82:1.2			
LG14	1.63:4.0	1.93:5.0	1.74:4.1		2.06:5.1	2.00:5.1	2.39:7.2	2.45:7.5		2.69:11.1
	3.16:1.5	3.67:1.3	3.22:0.4		3.41:2.9	3.11:2.2	3.65:1.0			
Komatiite	1.63:4.0	1.95:5.3	1.74:4.1		2.08:5.2	1.98:5.1	2.38:7.3	2.42:8.3	3.0:10.3	2.66:10.8
	3.16:1.9		3.18:0.5		3.40:1.1	3.18:4.2	3.69:1.0	2.91:0.2		
Peridotite	1.63:4.0		1.76:4.1		2.07:5.2	1.98:5.1	2.38:7.2			2.67:11.6
	3.14:1.7		3.18:0.2		3.36:1.1	3.15:5.7	3.80:0.4			
Olivine	1.62:4.0				2.07:5.4	2.00:5.2				2.69:12.4
	3.16:1.4				3.36:0.7	3.13:7.2				
Allende	1.63:4.0		1.74:4.1		2.05:5.2	1.98:5.0	2.37:7.1	2.44:8.0		2.68:11.2
	3.14:1.5		3.19:0.3		3.41:2.5	3.14:4.6	3.72:0.3			
Fayalite	1.62:4.0				2.00:4.7					2.65:12.0
	3.16:1.3				3.24:7.8					

For each cation is indicated: (first row) the cation–oxygen distance (in A), the mean number of oxygens around the cation; (second row) the cation–cation distance (in A) and the number of cations of the same species around each cation. For instance in rhyolite one reads in the column associated with Si: $R_{Si-O} = 1.63$ A, $N_O = 4.0$, $R_{Si-Si} = 3.16$ A and $N_{Si} = 3.3$. For oxygen atoms (last column) the first value corresponds to the oxygen–oxygen distance and the second value to the oxygen coordination number (e.g. for rhyolite, $R_{O-O} = 2.66$ A and $N_O = 7.0$).

a cubic simulation cell with periodic boundary conditions. Usual long range correction terms for dispersion interactions are added to the configurational energy and to the pressure. The long range coulombic interactions are accounted for by a Ewald sum (Allen and Tildesley, 1987) with a constant $\alpha L = 5$–7 (where α is the width of the charge distribution on each ion and L is the size of the simulation box) and a cut off distance (r_{cut}) of 10–11A, the summation in the reciprocal space being evaluated for all k vectors with $|k|\,L/2\pi < 6$–7. The parameters α, $|k|$ and r_{cut} were chosen in order to ensure a conservation of energy better than 10^{-5}. Calculations in the isothermal–isobaric NPT (using Nosé–Hoover algorithms) and microcanonical NVE ensembles were cross checked with production runs of 0.1–1. ns and long simulations runs of 10 ns (10^7 MD steps) were performed when evaluating time dependent properties. For a good compromise between accuracy and computational cost, we choose a system size of ~1000 atoms (see after). In the present study, the calculations were performed at zero pressure in order to compare with experimental data measured at atmospheric pressure. Concerning the statistical uncertainties, for a MORB composition evaluated at $T = 1673$ K and $P = 0$ we obtain the following results: in the NPT ensemble; $P = -0.06 \pm 4.93$ kbar, $T = 1673.8 \pm 42.4$ K and $\rho = 2.696 \pm 0.026$ g/cm^3; in the NVE ensemble; $P = -1.57 \pm 4.81$ kbar, $T = 1629.7 \pm 32.5$ K for $\rho = 2.677$ g/cm^3.

More generally, with $N \sim 1000$ atoms and for all investigated compositions the statistical fluctuations are the following: 0 ± 5 kbar for the pressure, $\Delta T/T = \pm 2\%$ for the temperature and $\Delta\rho/\rho = \pm 1\%$ for the density. To evaluate the influence of the system size on the melt properties, we have performed several test runs with $N = 8000$ atoms. No significant size effects were detected for the thermodynamic properties and the liquid structure (pair distribution functions) apart from the expected reduction of the statistical noise. Thus for MORB at 1673 K and $N = 8000$, the results in the NPT ensemble are very close to those obtained with $N = 1000$ (see above) namely; $P = 0.05 \pm 3.34$ kbar, $T = 1672.8 \pm 15.7$ K and $\rho = 2.688 \pm 0.023$ g/cm^3. Our findings are in agreement with other simulation studies (Rustad et al., 1990; Horbach et al., 1996; Huff et al., 1999) showing that static properties are barely affected by finite size effects. In contrast dynamical properties and especially structural relaxation near the glass transition temperature may depend on the size of the system.

3. Properties of the magmatic melts

3.1. Density, expansivity and heat capacity

In Fig. 1 are presented the evolution with temperature of the molar volume associated with the 11 silicate melts investigated here. All samples were first equilibrated in the liquid phase at high temperature (2500–3000 K) and around zero pressure and then cooled down to 400 K under isobaric condition with a sufficiently low cooling rate ($q = 2 \times 10^{11}$K/s) to ensure a quasi equilibrium state of the liquid upon cooling (we will discuss this point later on). The change of slope exhibited by the molar volume

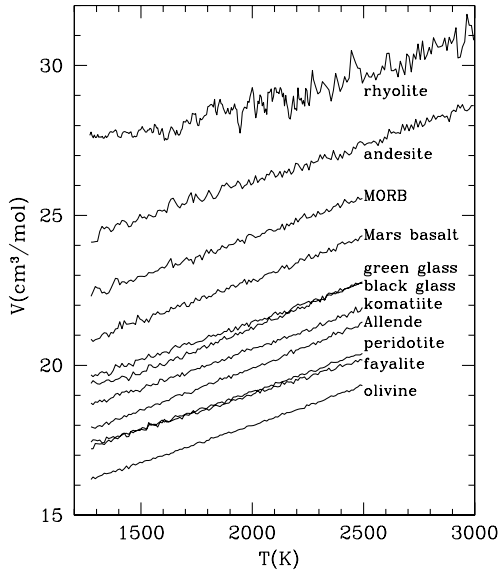

Fig. 1. Evolution with the temperature of the molar volume of the liquid silicates at zero pressure.

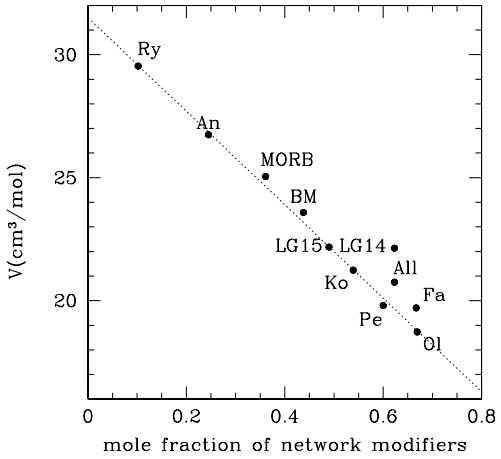

Fig. 2. Molar volume of the melt as function of the mole fraction of network modifiers. The full dots are for the liquid silicates at 2273 K, the dotted line being just a guide for the eye.

at low enough temperature indicates a liquid–glass transition (not shown). However, the evaluation of T_g by simulation is not an easy task and the results must be taken with great caution. As a matter of fact T_g depends on the applied cooling rate and on the size of the simulated sample (e.g. in Vollmayr et al., 1996). For these reasons an accurate determination of T_g is beyond the scope of this article and we focus our investigation on the liquid phase. Thus in using different cooling rates (from 10^{13} to 2×10^{10}K/s), different sizes of the system ($N = 1000$ and 8000 atoms) and by performing long simulation runs at fixed temperature and zero pressure we have carefully checked that the evolution with temperature of the molar volume presented in Fig. 1 for various composition is robust and describes the liquid phase of the corresponding simulated silicates as long as $T > 1273$ K. Below approximately 1273 K, the molar volume (and the enthalpy as well) becomes sensitive to the size of the sample and to the cooling rate, implying that the melt is entering the glassy phase.

In the context of Fig. 1, several points merit comments. The hierarchy of the molar volumes between the different silicates exhibits an almost linear dependence on the mole fraction of network-modifying cations (see Fig. 2), which is an indicator of the degree of depolymerisation of the melt (a related correlation with the NBO/T parameter was pointed out by Mysen and Richet (2005) for synthetic and natural melts). Only fayalite, LG14 and the Allende meteorite, the three most Fe-rich silicates, deviate slightly from this correlation. An interesting consequence of the above trend is that the solubility of a chemically inert volatile (e.g. rare gases) in these silicates is primarily governed by the free volume accessible to the solute into the melt (Guillot and Sarda, 2006) i.e., the smaller the molar volume of the melt the smaller the solubility of the volatile. Consequently, one expects that the solubility of a weakly interacting solute (e.g. helium or argon) in various silicate melts follows the hierarchy of the molar volumes illustrated in Fig. 1 (at least in the pressure range where the Henry law is approximately followed). For argon, solubility data of the literature support this view (Carroll and Stolper, 1993; Shibata et al., 1998; Marrocchi and Toplis, 2005).

Magma buoyancy is determined by density (g/cm^3). Therefore the density varies in the order,

$$\mathrm{Fa} > \mathrm{LG14} > \mathrm{All} > \mathrm{LG15} \sim \mathrm{Ol} \sim \mathrm{Pe} > \mathrm{BM} \sim \mathrm{Ko} > \mathrm{MORB} > \mathrm{An} > \mathrm{Ry}.$$

A comparison between our simulation results, available experimental data and theoretical models for multicomponent silicate liquids is presented in Fig. 3 for fayalite, peridotite, komatiite, MORB, and andesite. The agreement between experiment and simulation is of the order of 2% or less, which is quite remarkable considering the large composition range investigated and the uncertainties of various sources (numerical, experimental and those generated by slight differences in composition between simulation and experiment).

Another quantity easy to evaluate by simulation is the thermal expansivity. As seen in Fig. 1 the molar volume of the liquid increases linearly with temperature up to around 2500 K, irrespective of the composition of the melt (except for rhyolite which exhibits a more complex behavior). Above 2500 K, a non linear increase is expected (e.g. andesite in Fig. 1) due to the proximity of the liquid–vapor coexistence curve of these melts and the occurrence of the critical point at a much higher temperature.(Besides, a quick search by MD calculation locates the critical point for the investigated melts in the temperature range 5000–5500 K). The linearity of the molar volume with temperature over several hundreds of degrees has been observed for several liquid silicates (Nelson and Carmichael, 1979; Lange, 1996, 1997), at variance with the anorthite–diopside system (Knoche et al., 1992a,b; Toplis and Richet, 2000;

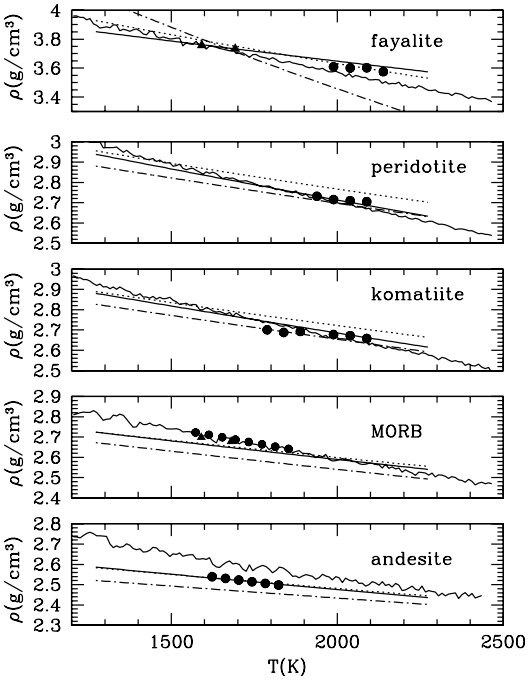

Fig. 3. Variation of the density with temperature for various liquid silicates. The wiggling lines are our simulation results, the straight lines are the predictions obtained from the model of Ghiorso and Kress (2004), the dotted lines are those from the model of Lange and Carmichael (1987) and the dashed-dotted lines are those from Bottinga et al. (1982, 1983). The full dots associated with fayalite, peridotite, and komatiite are experimental data of Courtial et al. (1997) while for fayalite, the data of Shiraishi et al. (1978) are also presented (triangles). In the case of MORB, comparisons are made with the data of Murase and McBirney (1973) for Columbia River basalt (triangles) and with the data of Nelson and Carmichael (1979) for Kilauea basalt (dots). For andesite, the data for an iron-free andesitic composition (sample No. 2 in Nelson and Carmichael, 1979) are shown (dots) after a slight correction accounting for the absence of iron in the experimental sample.

Gottsmann and Dingwell, 2002) and some titano-silicate liquids (Liu and Lange, 2001) where a stepping down of the thermal expansion is noticed when the temperature increases. In the latter cases the consequence is a net decrease of the thermal expansion coefficient ($\alpha_P = 1/V(dV/dT)_P$) in the liquid range, whereas for the natural melts investigated here this coefficient decreases very little ($\alpha_P \sim 1/V$), only 7–15% (according to the composition) between 1500 and 2500 K. Moreover, the simulation predicts that α_P increases roughly linearly with the mole fraction of network modifiers, the acidic melts presenting the lowest expansivity (see Table 3).

An accurate and simple route to evaluate the heat capacity (C_P) by MD calculation is to take the temperature derivative of the enthalpy at constant pressure. From an analytical fit of the enthalpy curve one deduces the variation of the heat capacity along the path going from the liquid to the glass. The C_P curve presents the expected S-shape in the neighborhood of T_g (not shown), with a more or less pronounced overshooting in the supercooled liquid before becoming essentially constant in the high temperature liquid. In the low temperature glass $C_P{}^g \to 3nR$ when $T \to 0$ (n is the mean number of atoms per oxide component), because the MD calculation is not corrected for quantum effects. Value of $C_P{}^l$ for the high temperature liquid above 2000 K (when C_P becomes essentially invariant) is given in Table 3 as function of composition. Although a number of C_P data exist in the literature for a rather large variety of silicate melts (Richet and Bottinga, 1986; Courtial and Richet, 1993; Navrotsky, 1995), they are scarce for natural melts or for synthetic ones mimicking a natural composition (e.g. Neuville et al., 1993). Therefore, we compare in Table 3 our MD results with those provided by the model of Stebbins et al. (1984) which assumes mixing of partial molar heat capacities associated with oxide components and which is valid only at superliquidus temperatures. Clearly the agreement between simulation and model is better for basic and ultrabasic melts than for acidic ones (andesite and rhyolite). But no systematic deviation is apparent, since in some cases the value of $C_P{}^l$ is overestimated by the simulation (e.g. rhyolite, andesite, MORB, Mars, green glass, and black glass) while it is underestimated in other cases (e.g. peridotite, olivine) and is in good agreement in a few cases (e.g. komatiite, allende, and fayalite).

3.2. Liquid structure

While the structure of binary and ternary silicate mixtures have been extensively investigated (for a survey see Mysen and Richet, 2005), the one of natural magmatic melts is less known especially in the high temperature liquid. In Table 4 we list the cation–oxygen, cation–cation and oxygen–oxygen mean distances of closest approach as well as the relevant coordination numbers evaluated at 2273 K (the coordination numbers are calculated by integrating the first peak of the corresponding pair distribution functions). These values are in excellent agreement with corresponding data of the literature: the reader can refer to the data compilation by Brown et al. (1995) presented in their Tables 1 and 3. The Si–O distance is found to be 1.62–1.63 A (uncertainty ± 0.005 A) for all melts. As expected (Cormier et al., 2001), the variation with temperature is very weak, and is less than 0.01 A between the glass at 400 K and the liquid at 2273 K. Silicon atoms are always coordinated to four oxygens in acidic, basic or ultrabasic melts. In the case of titanium, the Ti–O distance varies between 1.93 A in andesitic and basaltic melts and about 1.95 A in komatiite, the average number of coordinated oxygens amounting to 5.0–5.7. Aluminium and Fe^{3+} behave as network formers with a coordination number about 4.0–4.1 and 4.0–4.3, respectively, corresponding to a cation–oxygen distance about 1.74–1.76 A for Al and 1.82–1.84 A for Fe^{3+}.

The structural parameters associated with network modifying cations are generally more composition dependent than those for the network forming ones. Thus Fe^{2+} exhibits a distance to oxygen between 2.0 and 2.08 A,

the shortest distance being encountered in liquid fayalite with a coordination number around 4.7 as observed experimentally (Jackson et al., 1993), while other melts exhibit longer distances with Fe^{2+} coordinated to 4.8–5.2 oxygens. For Ca, the cation–oxygen distances in the simulated liquids are found close to those observed in soda lime aluminosilicate glasses (Cormier and Neuville, 2004), i.e. d(Ca–O) ~ 2.37–2.40 A with $N_O \sim 6.8–7.4$. For Mg the situation is more uniform with composition, d(Mg–O) ~ 1.98–2.0 A and $N_O \sim 4.9–5.2$, values which are in agreement with the structure data obtained by neutron and X-ray diffraction techniques in vitreous forsterite (Kohara et al., 2004; Wilding et al., 2004). As for the sodium and potassium cations, their mean distance to oxygen, d(Na–O) ~ 2.42–2.50 A and d(K–O) ~ 3.0–3.18 A, and the number of neighboring oxygens, about 7.5–8.3 for Na and 7.5–10.8 for K, are compatible with diffraction data from sodium and potassium silicate glasses and melts (Angeli et al., 2000; Majérus et al., 2004).

To further scrutinize the distribution of oxygens around Si, Al, Ti, Fe^{3+}, Fe^{2+}, and Mg, we have evaluated the abundance of n-coordinated species by doing a population analysis within the first shell of neighboring oxygen atoms. By convenience, this analysis is presented in Fig. 4 only for rhyolite, MORB, and Ti-rich lunar basalt (LG14), as mafic and ultramafic compositions exhibit essentially the same distributions than in MORB. As shown in Fig. 4, silicium is fourfold coordinated at 98.3% in rhyolite, at 97.2% in MORB and at 96.9% in LG14. A few percent of $^{[5]}$Si is also detected due to the high temperature of the simulated melts (2273 K). For all compositions investigated here, Al is clearly a network former with ~71–75% of $^{[4]}$Al, 4–12% of $^{[3]}$Al and 12–22% of $^{[5]}$Al, sixfold coordination being found in negligible proportion. These results are in agreement with spectroscopic data on alkaline-earth aluminosilicate glasses of related compositions (Wu et al., 1999; Neuville et al., 2004) which show a significant contribution of $^{[5]}$Al. It is noteworthy that the populations of $^{[4]}$Al and $^{[5]}$Al are relatively insensitive to the composition of silicate melts investigated here.

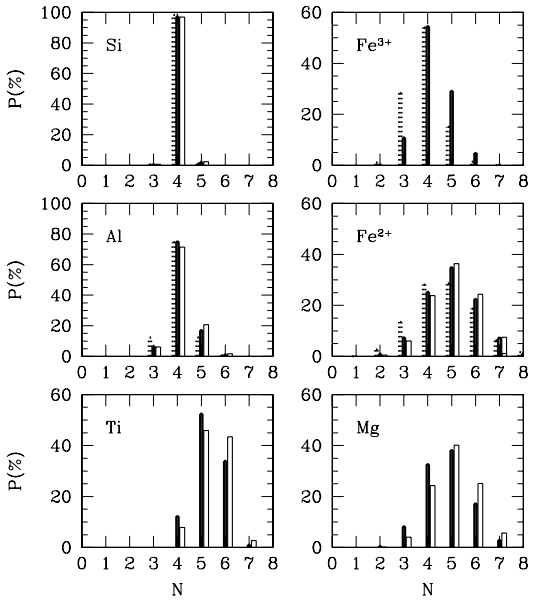

Fig. 4. Population analysis of cation coordination numbers in rhyolite (shaded sticks), in MORB (bold sticks) and in black glass (white sticks).

In andesite and MORB, Ti is found preferentially in 5-fold coordination (~52 to 54%) with a significant population of 6-fold coordinated sites (~31 to 34%), and a much weaker proportion of 4-fold coordinated sites (~12 to 14%). In the Ti-rich lunar basalt (16.4% of Ti in LG14) the abundances of $^{[5]}$Ti and $^{[6]}$Ti are close to each other (46% and 43%, respectively) whereas 4-fold coordination is rare (~8%). In investigating synthetic and natural volcanic glasses by XANES spectroscopy Farges and Brown (1997) found that $^{[5]}$Ti is the dominant species, but in less polymerized glasses of basaltic composition a significant amount of $^{[6]}$Ti is detected (30–50%) while in rhyolitic glasses 30–50% of the total Ti is attributed to $^{[4]}$Ti with $^{[6]}$Ti below the detection level (~10%). More generally X-ray absorption studies on Ti containing alkali/alkali-earth silicate glasses and melts (Farges et al., 1996; Henderson et al., 2002; Henderson and St-Amour, 2004) show that Ti containing silicate glasses can be considered as composition-dependent mixtures of 4-, 5- and 6-coordinated Ti, a low quenching rate favoring $^{[4]}$Ti over $^{[5]}$Ti. Clearly our results for the high temperature liquid are in accordance with these findings. However in titanosilicate glasses $^{[5]}$Ti is identified as a square based pyramid TiO_5 with a short Ti–O distance around 1.68 A and four long distances around 1.96 A (Cormier et al., 1998, 2001). A careful examination of our MD generated configurations does not show such a structure for TiO_5 and instead identifies five equivalent Ti–O bonds around 1.93 A. In summary, although Ti does not behave *stricto sensu* as a structure former in our simulated melts, the strong Ti–O bonds certainly exert a stabilizing effect on the network at variance with other network modifying cations.

In the case of iron, our population analysis (see Fig. 4) indicates that Fe^{3+} is found preferentially (~55%) in 4-fold coordination in rhyolite, andesite and MORB. This is in agreement with conventional wisdom that ferric iron in silicate melts is a structure former cation (see Mysen, 2006, and references therein). However, a significant amount (~29%) of ferric iron in 5-fold coordination is found in our simulated andesite and MORB while in rhyolite 3-fold coordination is favored (~28%) with respect to 5-fold coordination (~15%). The presence of 5-fold coordinated ferric iron is attested in silicic melts (Farges et al., 2004) and a minor proportion of 6-fold coordinated sites has also been reported in some volcanic glasses (Galoisy et al., 2001). In contrast, ferrous iron exhibits a broader range of oxygen coordination numbers around the most probable value (see Fig. 4). In all the investigated melts, 5-fold coordination is the most probable value except for rhyolite which exhibits a distribution slightly shifted towards lower coordination numbers. These features are in excellent

agreement with recent multi-spectroscopic studies (Jackson et al., 2005; Mysen, 2006) of ferrous iron in ferrosilicate glasses and with other simulation studies (Rossano et al., 2000a,b).

The distribution of oxygen coordination numbers for magnesium is very similar to that found for ferrous iron (see Fig. 4 and compare Mg with Fe^{2+}) where 5-fold coordination predominates. This distribution varies little from andesite to MORB and peridotite. However, in Fe-rich lunar basalt (LG14) and in olivine as well, the occurrence of 6-fold coordinated Mg is higher than in other melts (notice that the population of 4-fold coordination in those melts diminishes in the same proportion, see Fig. 4). This feature is likely due to low Si contents in these depolymerized melts which favor high coordination numbers for Mg and Fe^{2+}. The structure of our simulated Mg-rich olivine is quite similar to that reported for vitreous forsterite (Kohara et al., 2004) with a highly distorted network composed of interconnected SiO_4 tetrahedra and MgO_n polyhedra ($n = 4$, 5 and 6). Nevertheless the large difference in energy between Si–O and Mg–O bonds renders this network much more fragile in the liquid state than those associated with polymerized melts.

Interestingly, the oxygen–oxygen distance varies little with composition (2.65–2.69 A) when the oxygen coordination number (N_{OO}) is strongly composition dependent ($N_{OO} = 7$–12.4). More precisely, N_{OO} increases linearly with the mole fraction of network modifiers as illustrated in Fig. 5. This explains the observation made earlier (see Fig. 2) that the molar volume of the melt decreases linearly with the amount of network modifiers. As a matter of fact, the molar volume, a macroscopic quantity, is linearly correlated to N_{OO}, a microscopic quantity, as shown in Fig. 6. Thus, the higher the depolymerization of the melt the stronger the compaction of the oxygen atoms. The net result is a densification of the melt. To quantify the relationship between the depolymerization of the melt and its composition we have evaluated the network coordination number around Si (N_{Si}^T) that is the average number of network formers (Si + Al) around Si. We see in Fig. 7 that N_{Si}^T decreases gradually with composition from a value around 4.1 in rhyolite to a value as low as 1.3–1.4 in olivine and fayalite which means that a tetrahedral network cannot be formed in these liquids. The interesting point is that the decrease of N_{Si}^T as function of the mole fraction of network modifiers is essentially linear from acidic to ultrabasic melts.

Structural information on silicate glasses and liquids are commonly obtained from neutron diffraction, X-ray scattering and X-ray absorption experiments. Neutron diffraction is particularly interesting from a theoretical point of view because one has a direct access to the position of the nuclei within the melt, and the comparison with MD results is straightforward. Thus, the total radial distribution function available in neutron scattering experiment can be written as a weighted sum of partial pair

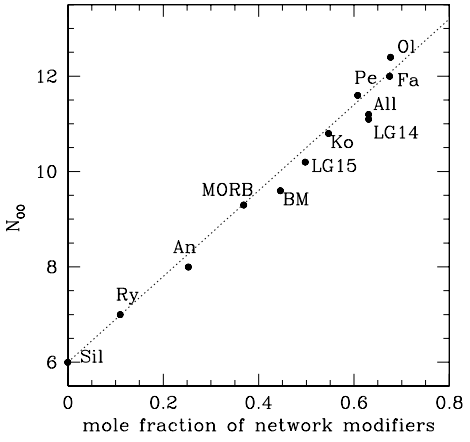

Fig. 5. Dependence of the oxygen coordination number on the melt composition at 2273 K. Values of N_{OO} are also given in the last column of Table 4. For the sake of completeness the value of N_{OO} in liquid silica (Sil) is shown in the figure. The dotted line is just a guide for the eye.

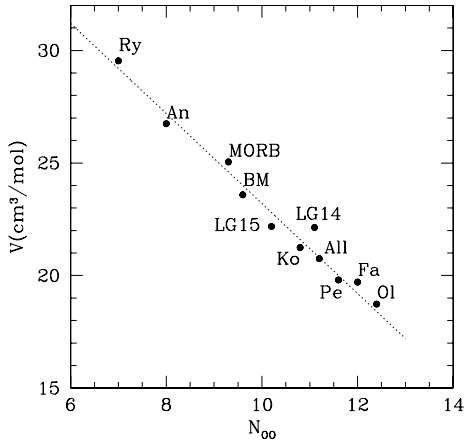

Fig. 6. Evolution of the molar volume of the melt at 2273 K with the oxygen coordination number. The dotted line is just a guide for the eye.

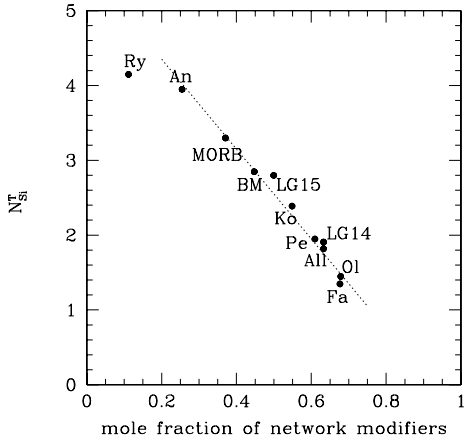

Fig. 7. Average number of network formers (Si + Al) around Si as function of the melt composition. Notice that acidic melts exhibit N_{Si}^T values close to that expected in pure silica melt (~4.0). The dotted line is just a guide for the eye.

distribution functions $g_{\alpha\beta}(r)$, where α and β run over all atoms of the melt,

$$G(r) = \sum_{\alpha,\beta} c_\alpha c_\beta b_\alpha b_\beta (g_{\alpha\beta}(r) - 1) \quad (3)$$

where c_α is the atomic concentration of the element α and b_α is the associated coherent neutron scattering length. In the case of a basaltic melt, nine different atomic elements have to be accounted for, which lead to 45 pair contributions in the definition of G(r) (in fact 55 if one considers Fe^{2+} and Fe^{3+} as two distinct chemical species). Moreover, due to the weighting factor ($c_\alpha\ c_\beta\ b_\alpha\ b_\beta$) in Eq. (3), the elements for which the atomic concentration is less than 10% barely contribute to the total distribution function. Although the isotopic substitution method can be used to enhance the contribution of some elements, most of the experimental works deal with simpler silicate melts as binary and ternary oxide mixtures. The present MD simulations give the opportunity to predict the profile of the neutron distribution function for any natural silicate melts. In Fig. 8, such a profile is presented for our simulated melts at 2273 K. The vertical dashed lines indicate the main cation–oxygen and cation–cation distances. The two main peaks located around 1.63 A (Si–O) and 2.66 A (O–O), respectively, decrease in magnitude from silicic to ultrabasic melts, while in between a feature appears which develops in a genuine peak for ferro-magnesian silicates. To better quantify the importance of elements other than Si and O atoms to $G(r)$, the global contribution coming from Si and O for each melt (dotted lines) is also reproduced in Fig. 8. For rhyolite, andesite and MORB it is hard to distinguish the influence of other elements. For the basalt of Mars, the higher contents in iron and magnesium become visible near 2.0 A. The Ti-rich content of the black lunar glass produces a deep minimum near 1.90 A, because the neutron scattering length of Ti is negative. As for the series LG15–Ko–Pe–All–Ol–Fa, the central peak around 2.0 A becomes all the more pronounced that the (Fe + Mg) content is high. Correspondingly, the peaks associated with Si and O atoms weaken from silicic to ultrabasic melts. In the case of liquid fayalite a supplementary peak appears around 3.24 A and corresponds essentially to Fe–Fe correlations. This peak has no visible counterpart in Mg-rich silicates like olivine and peridotite because of a less favorable scattering length for Mg (and Si as well) than for Fe ($b_{Mg}/b_{Fe} \sim 0.57$). Recent studies combining neutron and X-ray diffraction data (Kohara et al., 2004; Wilding et al., 2004) have characterized the structure in vitreous forsterite and found structural parameters which are in close agreement with those exhibited by our magnesium-rich melts. However, some features present in the experimental $G(r)$ function (e.g. the Mg–Si peak at 3.20 A) are barely visible in our simulated functions. This is likely due to a peak broadening induced by the high temperature of the simulated liquid (the experiments deal with rapid quenched glasses).

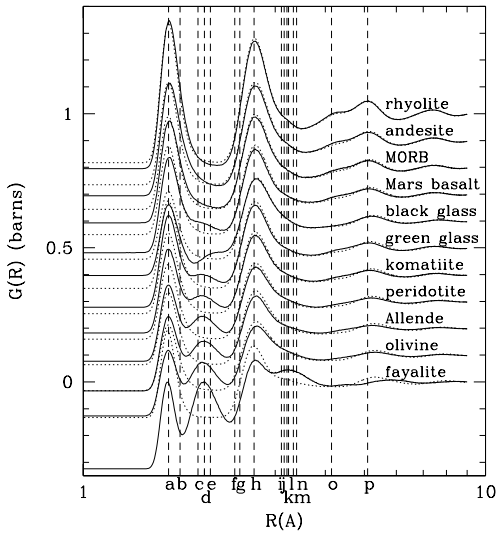

Fig. 8. Evolution of the neutron pair distribution function with melt composition. The full curves are the simulation results obtained with Eq. (3) while the dotted curves are the results obtained in considering only Si and O atoms. The vertical dashed lines point out some relevant atom–atom distances, namely: a = Si–O, b = Al–O, c = Ti–O, d = Mg–O, e = Fe^{2+}–O, f = Ca–O, g = Na–O, h = O–O, i = Mg–Mg, j = Si–Si, k = Al–Al, l = Fe^{2+}–Fe^{2+}, m = Mg–Si, n = Fe^{2+}–Si, o = Si–O (second neighbour) and p = O–O (second neighbour). Notice the logarithmic scale in abscissa.

3.3. Diffusivity and electrical conductivity

Diffusivity of ionic species into magmatic melts is of fundamental importance for viscous flow (Mungall, 2002), in rheology of volatile-bearing magmas (Watson, 1994) and for the interpretation of electrical conductivity data (Gaillard, 2004). Although an extensive literature on diffusion coefficients of ionic species in various silicate melts is available (Brady, 1995; Mungall, 2002; Zhabrev and Sviridov, 2003), the data base for natural melts is much more restricted. Mostly, the diffusivities of the major cations are not known altogether for a given melt, which prevents us from doing a proper comparison between different cations in the same melt. Here we have evaluated by MD simulation the ionic diffusivities in rhyolite, andesite, MORB, komatiite and peridotite in the temperature range 1473–2273 K (and down to 1273 K for MORB). The self-diffusion coefficient was computed from the MD run via the Einstein relation (Kubo, 1966),

$$D_s = \lim_{t\to\infty} \frac{1}{N_s} \sum_{i=1}^{N_s} \frac{\langle (\vec{r}_i(t) - \vec{r}_i(0))^2 \rangle}{6t} \quad (4)$$

where r_i is the position of the ith ion of species s, and where the bracket expresses an ensemble average taken over many origin times. Long simulation runs were performed (10 ns long and 10^3 origin times) to reduce the uncertainties on D values around ±5% for the most abundant ions (Si and O) and around ±40% for the less abundant cations (Ti, Fe^{3+}, Na, and K). The results are collected in Fig. 9

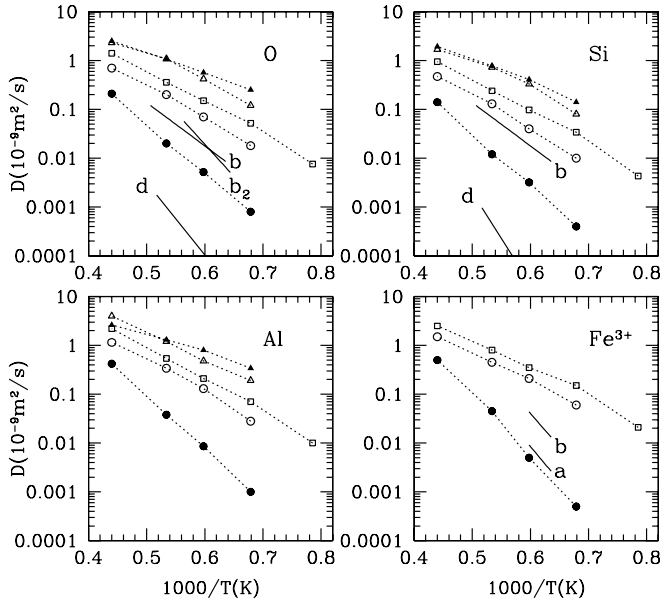

Fig. 9. Self-diffusion coefficients of network former ions in various silicate melts. The simulation results are: rhyolite (full dots), andesite (circles), MORB (squares), komatiite (empty triangles), peridotite (full triangles). The dotted curves are just a guide for the eye. Also shown for comparison are the experimental data (straight lines) for O and Si in basaltic liquid (line *b*) by Lesher et al. (1996) and in dacitic liquid (line *d*) by Tinker and Lesher (2001) as also as the data of Canil and Muehlenbachs (1990) for O in another basaltic composition (line b2). For Fe^{3+} are shown the data of Henderson et al. (1985) in basaltic and andesitic melts (see line *b* and *a*, respectively). For simulated rhyolite, where the temperature behavior of the diffusivities is found to be Arrhenius-like, the activation energies for O, Si, Al and Fe^{3+} self-diffusion are equal to 191.4, 209.0, 216.9, and 191.5 kJ/mol, respectively, values which can be compared to the activation energies of O (223 ± 29 kJ/mol) and Si (200 ± 28 kJ/mol) measured in a dacitic liquid (Tinker and Lesher, 2001; Tinker et al., 2002).

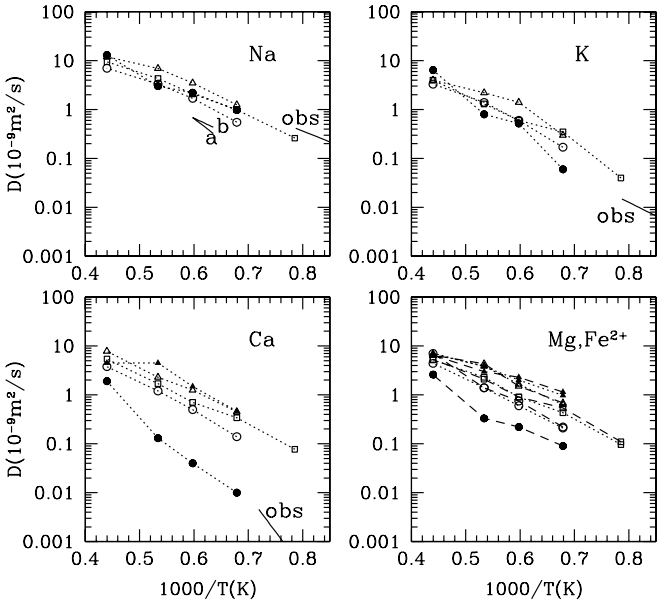

Fig. 10. Self-diffusion coefficients of network modifier cations in various silicate melts. Symbols are the same as in Fig.10. The self diffusion of Na, K, and Ca in obsidian measured by Jambon (1982) is shown for comparison (see lines *obs*) as also as the diffusivity of Na in andesitic and basaltic liquids (lines *a* and *b*, respectively) as reported by Henderson et al. (1985).

for network former ions and in Fig. 10 for network modifier cations, respectively. Concerning the former ones (O, Si, Al and Fe^{3+}), the more silicic the melt the smaller the diffusion coefficients. This finding is in agreement with the trend shown by the viscosity in these melts (see Fig.1 in Giordano and Dingwell, 2003). For Ti in rhyolite and andesite the calculated diffusivity (not shown) is slightly greater than that evaluated for Si whereas in MORB, komatiite, and peridotite the Ti diffusivity is slightly smaller than that of Si. Moreover, the temperature behavior of the diffusion coefficients is Arrhenius-like in liquid rhyolite whereas it is not so in other melts. This feature can be related to the greater fragility of basic and ultrabasic melts as compared with a strong glass former like rhyolite. Notice that the diffusion coefficient of Fe^{3+} is close to that of Al^{3+} both in rhyolite and in MORB which confirms its role as a network former cation in these melts.

Self-diffusion of oxygen and silicon has been measured in basaltic liquids (Canil and Muehlenbachs, 1990; Lesher et al., 1996) and in a dacitic liquid (Tinker and Lesher, 2001). In basalt, the simulation overestimates D_{Si} and D_O by an order of magnitude at 1500 K and by a factor of four at 2000 K. In the dacitic liquid, which is roughly comparable to our simulated rhyolite, the overestimation is even greater with almost two orders of magnitude at 1500 K and one order of magnitude around 2000 K. Similarly, the values of Henderson et al. (1985) for the diffusivity of Fe^{3+} in basaltic and andesitic melts are much smaller than our evaluations (see Fig. 9), the lower the temperature the greater the deviation. These discrepancies suggest that the simulated liquids, especially those with high SiO_2 contents, are not sufficiently viscous. Incidentally, the same problem is encountered with strong glass formers like silica and germania (Micoulaut et al., 2006) where the commonly used empirical potentials for these systems overestimate by several orders of magnitude the diffusivity of silicon and oxygen atoms in the temperature range $T_g/T \sim 0.5$–1.

The case of the network modifying cations is rather different (Fig. 10). Even if sodium is always the most diffusive cation ($D_{Na} > D_K \geqslant D_{Fe^{2+}} \geqslant D_{Mg} \geqslant D_{Ca}$), the diffusion coefficients are less dependent on composition and are close to each other. However, contrarily to sodium and potassium, Ca, and Fe^{2+} diffuse more slowly in rhyolite than in basic and ultrabasic melts. Existing data of the literature confirm these trends. Thus a simple extrapolation (Arrhenius-like) at high temperature, of the diffusion coefficients for Na, K, and Ca obtained by Jambon (1982) in a granitic obsidian between 400 and 1200 K, matches our evaluations for these cations in liquid rhyolite (see Fig. 10). In the same way, in spite of a slight overestimation, the simulation reproduces the observation made by Henderson et al. (1985) that the diffusivities of sodium in andesitic and basaltic liquids are close to each other. It is interesting to

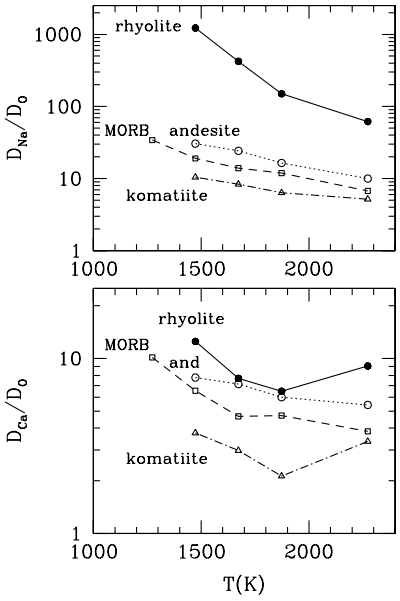

Fig. 11. Relative diffusivity of sodium (upper panel) and calcium (lower panel) with respect to oxygen self-diffusion as function of temperature. The lines are just guides for the eye.

compare the diffusivity of network modifiers with respect to that of network formers as function of the composition of the melt. As illustrated in Fig. 11, the ratio D_{Na}/D_O varies between ~60 and ~1200 in rhyolite when the temperature decreases from 2273 to 1473 K, between ~10 and ~30 in andesite, between ~7 and ~20 in MORB and between ~5 and ~10 in komatiite: the more basic the composition the smaller the ratio and the smaller the variation with temperature. In contrast, the ratio D_{Ca}/D_O exhibits much smaller values (roughly between 2 and 10) for all composition.

Information on partial melting occurring in the Earth mantle can be extracted from in situ magnetotelluric and geomagnetic data provided that the electrical conductivity of magmatic melts and rocks is known (Xu et al., 2000; Hoffmann-Rothe et al., 2001; Park and Ducea, 2003; Booker et al., 2004). A number of electrical conductivity data in natural silicate melts are available (see Table 1 in Partzsch et al., 2000) and it is interesting to test the ability of our simulated melts to reproduce these data. Within the framework of linear response theory (Kubo, 1966), the electrical conductivity of an ionic liquid is given by,

$$\sigma = \frac{1}{3kTV}\int_0^\infty \langle \vec{j}(t).\vec{j}(0)\rangle \mathrm{d}t \tag{5}$$

where the charge current $\vec{j}$ is defined by

$$\vec{j}(t) = \sum_{i=1}^{N} z_i \vec{v}_i(t) \tag{6}$$

with k the Boltzmann constant, V the volume of the sample, z_i the charge carried by the ion i, $\vec{v}_i$ its velocity and N the total number of ions. In Eq. (5), $\langle - \rangle$ denotes a canonical averaging.

Alternatively, this expression can be rewritten in a more convenient form in terms of the mean square displacement of the ions,

$$\sigma = \frac{1}{kTV}\left\langle \frac{\left|\sum_{i=1}^{N} z_i(\vec{r}_i(t) - \vec{r}_i(0))\right|^2}{6t} \right\rangle_{t\to\infty} \tag{7}$$

A widely used expression is the Nernst–Einstein (NE) approximation which assumes that each ion is mobile independently from each other. In this case Eq. (7) writes,

$$\sigma_{NE} = \frac{1}{kTV}\sum_s N_s z_s^2 D_s \tag{8}$$

where N_s is the number of ions of species s, and D_s the self-diffusion coefficient associated with the ionic species s. This expression, although approximate, is often used because the total electrical conductivity can be interpreted as a sum of ionic conductivities. However, the exact expression Eq. (7) of the conductivity is given by,

$$\sigma = H\sigma_{NE} \tag{9}$$

where H, the so-called Haven ratio, expresses the cross correlations between charge carriers within the melt. For information notice that in molten salts, $H < 1$, because the anion–cation interactions tend to decrease the conductivity.

We have evaluated by simulation via Eq. (7), the conductivity in the liquid state of rhyolite, andesite, MORB, komatiite, and peridotite. The results are presented in Fig. 12 and are compared with experimental data for analog

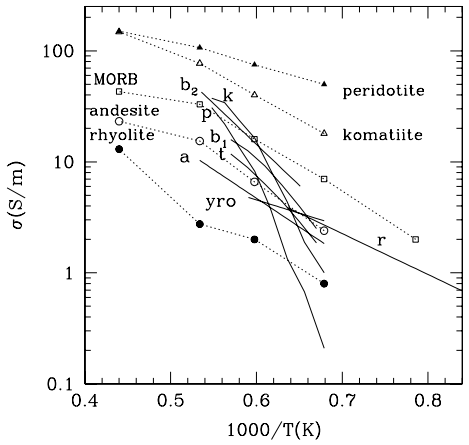

Fig. 12. Electrical conductivity of various silicate melts. Symbols are the same as in Figs. 10 and 11, and the dotted curves are guidelines. The full curves marked by letters represent experimental data of the literature: *k*, komatiite (Rai and Manghnani, 1978); *p*, peridotite (Rai and Manghnani, 1978); b_1, basalt (Waff and Weill, 1975); b_2, basaltic liquid (Presnall et al., 1972); *t*, Hawaïan tholeiite (Tyburczy and Waff, 1983), *a*, andesite (Waff and Weill, 1975); *yro*, Yellowstone rhyolite obsidian (Tyburczy and Waff, 1985); *r*, rhyolite (Gaillard, 2004). Notice that for komatiite (*k*) and peridotite (*p*) the sharp increase of the experimental conductivities is attributed to the evolution of the melt fraction with temperature.

melts. The calculations show that the more depolymerised the melt the higher the conductivity ($\sigma_{Ry} < \sigma_{An} < \sigma_{MORB} < \sigma_{Ko} < \sigma_{Pe}$). This trend is also observed in the experimental data, at least in the high temperature liquid (see Rai and Manghnani, 1977, 1978; Tyburczy and Waff, 1985). However, for partially molten silicates Gaillard and Marziano (2005) reach a different conclusion. One notices that, generally, the experimental conductivities increase sharply (~2 orders of magnitude) upon heating between solidus and liquidus temperatures (i.e. between 1403 and 1536 K for basalt and between 1470 K and ~1690 K for a garnet peridotite, see Presnall et al. (1972) and Rai and Manghnani (1978)). This abrupt increase is attributed to a partial melting of mafic rocks (Presnall et al., 1972; Rai and Manghnani, 1978; Maumus et al., 2005) and consequently, only the conductivity data measured at superliquidus temperatures have to be compared with our simulation results. Taking into account the statistical uncertainties of our calculations (roughly a factor of two for the conductivity), the variation in composition between experimental and simulated samples and the influence of partial melting on the measurements, we conclude that the simulation gives a reasonable estimation of the conductivity of natural silicate melts at superliquidus temperatures.

In order to estimate the contribution of each ionic species to the conductivity of the melt, we have evaluated the ionic conductivities associated with the Nernst–Einstein approximation see Eq. (8). This approximation leads to total conductivities very similar to the ones presented in Fig. 12 except that the values are systematically overestimated by a factor between 1 and 3. In fact the Haven ratio, defined in Eq. (9), is found to lie between 1 and 0.3, and exhibits no clear variation with composition nor with the temperature. To verify the conventional view that in Na-bearing melts, sodium is considered as the dominant charge carrier, we have evaluated its contribution to the conductivity in the high temperature liquid through the ratio σ_{Na}/σ, where σ_{Na} is obtained from the NE expression (8) applied to sodium ions only. As shown in Fig. 13, sodium plays practically no role in liquid komatiite (~ 1%), a modest role in andesitic and basaltic liquids (less than ten percent), and a predominant role in liquid rhyolite (~85% around 1500 K). The latter finding is the consequence of the very large mobility of sodium with respect to other ions and especially the network former ones (see Fig. 11). So our calculations confirm the experimental deduction (Gaillard, 2004) that Na is the dominant charge carrier in rhyolitic melt. However, we have to re-emphasize that our simulated rhyolite is much less viscous that the real one in this temperature range (less than 1 Pa S at 2273 K instead of ~100 Pa S) and consequently the contribution of sodium to the conductivity is certainly underestimated.

In andesitic, basic, and ultrabasic liquids, the contribution of other ions (network modifiers and network formers) is non-negligible (e.g. Ca in Fig. 13). Notice

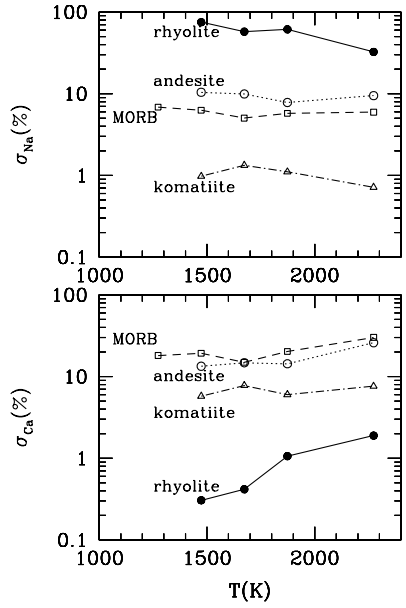

Fig. 13. Relative contribution of sodium (upper panel) and calcium (lower panel) to the electrical conductivity of the melt as function of temperature. The sodium and calcium conductivities were estimated in the framework of the Nernst–Einstein approximation (see text).

that a similar conclusion was reached in a recent experimental study of ternary $CaO–Al_2O_3–SiO_2$ compositions (Gruener et al., 2001), where the silica content was found to be the principal parameter that governs the temperature dependence of the conductivity in the liquid phase.

4. Conclusion

In implementing into a molecular dynamics simulation code a simple interionic potential developed to describe the KNCMFATS system, it has been possible to reproduce satisfactorily a number of thermodynamic, structural and transport properties of a representative set of natural silicate melts. An important conclusion reached in this study is the good transferability of the interionic potential from felsic to ultramafic compositions. However, this transferability becomes less accurate for compositions with very high silica contents (rhyolitic composition and beyond) and for iron-rich silicates (e.g. fayalite). Between these two limiting cases (i.e. for most of the magmatic liquids) we believe that our MD simulation is a useful, accurate and inexpensive (in computer time) theoretical tool to improve our understanding of natural magmatic melts. A great advantage of the simulation is that it permits us to make the link between macroscopic properties and microscopic structure and dynamics. It is also quite rewarding that several basic behaviors, characteristic of natural melts, show up readily in the simulations. An example is the almost perfect linear dependence of the molar volume of the silicate liquids on the temperature range 1300–2500 K. Another

advantage of the simulation is its ability to evaluate quantities which are not easily measurable as the cation coordination numbers. In the same way, when it is the question to evaluate the contribution of the different ionic species to the conductivity of natural melts, the simulation points out that sodium is the dominant charge carrier for highly silicic melts like rhyolite except at very high temperatures when the viscosity is sufficiently low (~1 Pa S or less) and the network forming ions become highly mobile. At temperatures prevailing at depth in the upper mantle (1373–1673 K) where magmatism takes place, as under oceanic ridges, the conductivity of a magma in the course of crystallization was recently investigated and attributed essentially to the mobility of sodium through the melt (Gaillard and Marziano, 2005). Although this result seems in contradiction with our simulation data on basaltic melts it is noteworthy that the residual liquid changes composition (from basalt to andesite to dacite liquid) in the course of crystallization, an effect which is not accounted for in the simulation. Future simulation studies using much larger system size might allow evaluating the conductivity of a mafic sample at different melt fraction. However that may be, to be useful our model potential has to prove its ability to describe the pressure behavior of natural melts (equation of state, structural reorganization and modification of transport properties under pressure). This is what we will show in part II of this series.

Acknowledgment

The constructive review of P. Richet is acknowledged with thanks.

Associate editor: Bjorn Mysen

Appendix

With the aim of investing a broad variety of silicate melts of geological interest, we have simulated the following natural compositions (see Table 1 for their chemical composition).

1. Rhyolite (Ry). This natural rhyolitic obsidian has been investigated by Gaillard (2004) and Gaillard et al. (2003). Its glass transition temperature and its electrical conductivity have been measured by these authors. This is the most felsic composition investigated here.

2. Andesite (An). An andesite from Unzen volcano (Chen et al., 1993) was chosen as representative of intermediate igneous rocks.

3. Mid-ocean ridge basalt (MORB). We selected a basalt from the mid-atlantic ridge at Kane (MARK area), one of the most thoroughly studied locations on a slow spreading ridge. We have simulated the basaltic composition of the sample TK21B dredges at 3160 m depth in the neovolcanic zone, remote from the Kane transform fault (Reynolds and Langmuir, 1997). For the sake of completeness we have also simulated an average MORB evaluated from 94 selected ocean floor basalt analyses (Cann, 1971) as also as a tholeiite from the Vema fault zone in central atlantic (Melson and Thomson, 1971). No significant difference was found when comparing the simulated properties of all these basalts. So only the results obtained with the TK21B sample are discussed here.

4. Basalt from Mars (BM). Three basaltic rocks have been recently analyzed by the Spirit rover in Gusev crater on Mars (McSween et al., 2004). These basalts are iron-rich with low SiO_2 and high MgO contents indicating a primitive nature. By convenience we simulated the composition of the rock named Humphrey.

5. Apollo 15 lunar green glass (LG15). The pristine glasses bring back from the surface of the moon are compositionally distinct from terrestrial magmas (Delano, 1986). They show a wide range of TiO_2 contents (0.3–16.4 wt%), high FeO contents (16–25 wt%) and a high Mg/(Mg + Fe) ratio. They possibly represent the most primitive mare basalt compositions available. The Apollo 15 green glass is the most Ti-poor and shows the highest Mg/(Mg + Fe) ratio of the lunar glasses. Incidentally, it shares some compositional similarities with the basaltic rocks of Gusev crater on Mars.

6. Apollo 14 lunar black glass (LG14). This sample has the highest TiO_2 content of the pristine mare glasses (the opposite of the green glass). Circone and Agee (1996) found that it is significantly more compressible than other basic and ultrabasic silicate liquids, and suggested that this peculiarity could be related to its high TiO_2 content.

7. Komatiites (Ko). Komatiites are ultramafic lavas produced most commonly during the early Earth. The presently investigated komatiite is a 2.8 b.y.-old extrusive from Belingwe (Zimbabwe), for which static compression measurements in the liquid phase have been reported (Agee and Walker, 1988).

8. Peridotite (Pe). PHN1611 is a primitive mantle peridotite (a garnet lherzolite, Nixon and Boyd, 1973) representing the common upper mantle composition. The evolution of its density with temperature (at one bar) and with pressure as well, has been measured in the liquid phase (Courtial et al., 1997; Ohtani et al., 1998; Suzuki and Ohtani, 2003).

9. Allende meteorite (All). This carbonaceous chondrite (CV3), fallen in 1969, is considered as one of the most primitive objects yet sampled in the solar system. Some authors (Agee, 1990; Asahara et al., 2004) advocate that the Allende meteorite is an interesting candidate as a building block of primordial Earth during the accretion period.

10. Olivine (Ol). This is a major mineral of the upper mantle. We selected the widely used San Carlos olivine with a composition ($(Mg_{0.9}Fe_{0.1})_2SiO_4$) close to the Mg-rich end member forsterite.

11. Fayalite (Fa). Fe_2SiO_4 is the iron-rich end member of $(Mg,Fe)_2SiO_4$, the major constituent of the earth's mantle.

References

Agee, C.B., 1990. A new look at differentiation of the Earth from melting experiments on the Allende meteorite. *Nature.* **346**, 834–837.

Agee, C.B., Walker, D., 1988. Static compression and olivine flotation of ultrabasic silicate liquid. *J. Geophys. Res.* **93**, 3437–3449.

Allen, M.P., Tildesley, D.J., 1987. *Computer Simulation of Liquids*. Oxford University Press, Oxford.

Angeli, F., Delaye, J.-M., Charpentier, T., Petit, J.-C., Ghaleb, D., Faucon, P., 2000. Influence of glass chemical composition on the Na–O bond distance: a ^{23}Na 3Q-MAS NMR and molecular dynamics study. *J. Non-Cryst. Solids* **276**, 132–144.

Angell, C.A., Cheeseman, P., Tamaddon, S., 1983. Water-like transport property anomalies in liquid silicates investigated at high T and P by computer simulation techniques. *Bull. Mineral.* **106**, 87–97.

Asahara, Y., Kubo, T., Kondo, T., 2004. Phase relations of carbonaceous chondrite at lower mantle conditions. *Phys. Earth Planet. Int.*, 143–144.

Belashchenko, D.K., 1996. Computer simulation on non-crystalline oxides MeO and Me_2O_3. *J. Non-Cryst. Solids*, 205–207.

Benoit, M., Ispas, S., Jund, P., Jullien, R., 2000. Model of silica glass from combined classical and ab-initio molecular-dynamics simulations. *Eur. Phys. J. B* **13**, 631–636.

Bockris, J.O'M., Tomlinson, J.W., White, J.L., 1956. The structure of liquid silicates: partial molar volumes and expansivities. *Trans. Faraday Soc.* **53**, 299–310.

Booker, J.R., Favetto, A., Pomposiello, M.C., 2004. Low electrical resistivity associated with plunging of the Nazca flat slab beneath Argentina. *Nature.* **429**, 396–403.

Bottinga, Y., Weill, D.F., 1970. Density of liquid silicate systems calculated from partial molar volumes of oxide components. *Am. J. Sci.* **269**, 169–182.

Bottinga, Y., Richet, P., Weill, D.F., 1983. Calculation of the density and thermal expansion coefficient of silicate liquids. *Bull. Mineral.* **106**, 129–138.

Bottinga, Y., Weill, D.F., Richet, P., 1982. Density calculations for silicate liquids. I Revised method for alumino silicate compositions. *Geochim. Cosmochim. Acta* **46**, 909–919.

Brady, J.B., 1995. Diffusion data for silicate minerals, glasses and liquids. In: Ahrens, T.J. (Ed.), *Mineral Physics and Cristallography: A handbook of Physical Constants*. AGU, Washington DC, pp. 269–290.

Brown Jr., G.E., Farges, F., Calas, G., 1995. X-ray scattering and X-ray spectroscopy studies of silicate melts. *Rev. Mineral.* **32**, 317–410.

Canil, D., Muehlenbachs, 1990. Oxygen diffusion in Fe-rich basalt melt. *Geochim. Cosmochim. Acta* **54**, 2947–2951.

Cann, J.R., 1971. Major elements variations in ocean-floor basalts. *Philos. Trans. R. Soc. Lond. A* **268**, 495–505.

Caro, G., Bourdon, B., Wood, B.J., Corgne, A., 2005. Trace element fractionation in Hadean mantle generated by melt segregation from a magma ocean. *Nature.* **436**, 246–249.

Carroll, M.R., Stolper, E.M., 1993. Noble gas solubilities in silicate melts and glasses: new experimental results for argon and the relationship between solubility and ionic porosity. *Geochim. Cosmochim. Acta* **57**, 5039–5051.

Chen, C.H., DePaolo, D.J., Nakada, S., Shieh, Y.-N., 1993. Relationship between eruption volume and neodymium isotopic composition at Unzen volcano. *Nature.* **362**, 831–834.

Circone, S., Agee, C.B., 1996. Compressibility of molten high-Ti mare glass. Evidence for crystal–liquid density inversions in the lunar mantle. *Geochim. Cosmochim. Acta* **60**, 2709–2720.

Cormier, L., Gaskell, P.H., Calas, G., Soper, A.K., 1998. Medium-range order around titanium in a silicate glass studied by neutron diffraction with isotopic substitution. *Phys. Rev. B* **58**, 11322–11330.

Cormier, L., Calas, G., Neuville, D.R., Bellissent, R., 2001. A high temperature neutron diffraction study of a titanosilicate glass. *J. Non-Cryst. Solids*, 510–516.

Cormier, L., Neuville, D.R., 2004. Ca and Na environments in Na_2O–CaO–Al_2O_3–SiO_2 glasses: influence of cation mixing and cation-network interactions. *Chem. Geol.* **213**, 103–113.

Courtial, Ph., Richet, P., 1993. Heat capacity of magnesium alumino-silicate melts. *Geochim. Cosmochim. Acta* **57**, 1267–1275.

Courtial, Ph., Ohtani, E., Dingwell, D.R., 1997. High-temperature densities of some mantle melts. *Geochim. Cosmochim. Acta* **61**, 3111–3119.

Delano, J.W., 1986. Pristine lunar glasses: criteria, data and implications. *J. Geophys. Res.* **91**, D210–D213.

Delaye, J.M., Louis-Achille, V., Ghaleb, D., 1997. Modeling oxide glasses with Born–Mayer–Huggins potentials: effect of composition on structural changes. *J. Non-cryst. Solids* **210**, 232–242.

Delaye, J.M., Cormier, L., Ghaleb, D., Calas, G., 2001. Investigation of multicomponent silicate glasses by coupling WAXS and molecular dynamics. *J. Non-cryst. Solids*, 293–295.

Demilrap, E., Cagin, T., Goddard III, W.A., 1999. Morse stretch potential charge equilibrium force field for ceramics : application to the quartz-stishovite phase transition and to silica glass. *Phys. Rev. Lett.* **82**, 1708–1711.

Elkins-Tanton, L.T., Hager, B.H., 2005. Giant meteoroid impacts can cause volcanism. *Earth Planet. Sci. Lett.* **239**, 219–232.

Farges, F., Brown Jr., G.E., 1997. Coordination chemistry of Ti(IV) in silicate glasses and melts: IV. XANES studies of synthetic and natural volcanic glasses and tektites at ambient temperature and pressure. *Geochim. Cosmochim. Acta* **61**, 1863–1870.

Farges, F., Brown Jr., G.E., Navrotsky, A., Gan, H., Rehr, J.R., 1996. Coordination chemistry of Ti(IV) in silicate glasses and melts: III. Glasses and melts from ambient to high temperatures. *Geochim. Cosmochim. Acta* **60**, 3055–3065.

Farges, F., Lefrère, Y., Rossano, S., Berthereau, A., Calas, G., Brown Jr., G.E., 2004. The effect of redox state on the local structural environment of iron in silicate glasses: a combined XAFS spectroscopy, molecular dynamics, and bond valence study. *J. Non-Cryst. Solids* **344**, 176–188.

Feuston, B.P., Garofalini, S.H., 1988. Empirical three-body potential for vitreous silica. *J. Chem. Phys.* **89**, 5818–5824.

Frenkel, D., Smit, B., 1996. *Understanding Molecular Simulation: From Algorithms to Applications*. Elsevier, Amsterdam.

Gaillard, F., Schmidt, B., Mackwell, S., McCammon, C., 2003. Rate of hydrogen-iron redox exchange in silicate melts and glasses. *Geochim. Cosmochim. Acta* **67**, 2427–2441.

Gaillard, F., 2004. Laboratory measurements of electrical conductivity of hydrous and dry silicic melts under pressure. *Earth Planet. Sci. Lett.* **218**, 215–228.

Gaillard, F., Marziano, G.I., 2005. Electrical conductivity of magma in the course of crystallization controlled by their residual liquid composition. *J. Geophys. Res.* **110**, B06204.

Galoisy, L., Calas, G., Arrio, M.A., 2001. High-resolution XANES spectra of iron in minerals and glasses: structural information from the pre-edge region. *Chem. Geol.* **174**, 307–319.

Ganster, P., Benoit, M., Kob, W., Delaye, J.-M., 2004. Structural properties of a calcium alumino-silicate glass from molecular dynamics simulations: a finite size effects study. *J. Chem. Phys.* **120**, 10172–10181.

Ghiorso, M., 2004. An equation of state for silicate melts. Parts I, III, IV. *Am. J. Sci.* **304**, 637–678, 752–810, 811–838.

Ghiorso, M., Kress, V.C., 2004. An equation of state for silicate melts. Part II. *Am. J. Sci.* **304**, 679–751.

Giordano, D., Dingwell, D.B., 2003. Non-Arrhenian multicomponent melt viscosity: a model. *Earth Planet. Sci. Lett.* **208**, 337–349.

Gottsmann, J., Dingwell, D.B., 2002. Thermal expansivities of super-cooled haplobasaltic liquids. *Geochim. Cosmochim. Acta* **66**, 2231–2238.

Gruener, G., De Sousa Meneses, D., Odier, P., Loup, J.P., 2001. Influence of the network on conductivity in ternary CaO–Al_2O_3–SiO_2 glasses and melts. *J. Non Cryst. Sol.* **281**, 117–124.

Guillot, B., Sarda, Ph., 2006. The effect of compression on noble gas solubility in silicate melts and consequences for degassing at mid-ocean ridges. *Geochim. Cosmochim. Acta* **70**, 1215–1230.

Henderson, G.S., Liu, X., Fleet, M.E., 2002. A Ti L-edge X-ray absorption study of Ti-silicate glasses. *Phys. Chem. Miner.* **29**, 32–42.

Henderson, P., Nolan, J., Cunningham, G.C., Lowry, R.K., 1985. Structural controls and mechanisms of diffusion in natural silicate melts. *Contrib. Mineral. Petrol.* **89**, 263–272.

Henderson, G.S., St-Amour, J.C., 2004. A Si K-edge XANES study of Ti containing alkali/alkali-earth silicate glasses. *Chem. Geol.* **213**, 31–40.

Herzbach, D., Binder, K., Müser, M.H., 2005. Comparison of model potentials for molecular-dynamics simulations of silica. *J. Chem. Phys.* **123**, 124711–124720.

Hoffmann-Rothe, A., Ritter, O., Haak, V., 2001. Magnetotelluric and geomagnetic modelling reveals zones of very high electrical conductivity in the upper crust of Central Java. *Phys. Earth Planet. Int.* **124**, 131–151.

Horbach, J., Kob, W., Binder, K., Angell, C.A., 1996. Finite size effects in simulations of glass dynamics. *Phys. Rev. E* **54**, R5897–R5900.

Huang, C., Cormack, A.N., 1990. The structure of sodium silicate glass. *J. Chem. Phys.* **93**, 8180–8186.

Huff, N.T., Demilrap, E., Çagin, T., Goddard III., W.A., 1999. Factors affecting molecular dynamics simulated vitreous silica structures. *J. Non-Cryst. Solids* **253**, 133–142.

Jackson, W.E., Farges, F., Yeager, M., Mabrouk, P.A., Rossano, S., Waychunas, G.A., Solomon, E.I., Brown Jr., G.E., 2005. Multi-spectroscopic study of Fe(II) in silicate glasses: implications for the coordination environment of Fe(II) in silicate melts. *Geochim. Cosmochim. Acta* **69**, 4315–4332.

Jackson, W.E., Mustre de Leon, J., Brown Jr., G.E., Waychunas, G.A., Condradson, S.D., Combes, J.M., 1993. High-temperature XAS study of Fe_2SiO_4 liquid: reduced coordination of ferrous iron. *Science.* **262**, 229–233.

Jambon, A., 1982. Tracer diffusion in granitic melts: experimental results for Na, K, Rb, Cs, Ca, Sr, Ba, Ce, Eu to 1300 °C and a model of calculation. *J. Geophys. Res.* **87**, 10797–10810.

Kieffer, J., Angell, C.A., 1989. Structural incompatibilities and liquid-liquid phase separation in molten binary silicates: a computer simulation. *J. Chem. Phys.* **90**, 4982–4991.

Knoche, R., Dingwell, D.B., Webb, S.L., 1992a. Temperature-dependent thermal expansivities of silicate melts: the system anorthite-diopside. *Geochim. Comochim. Acta* **56**, 689–699.

Knoche, R., Dingwell, D.B., Webb, S.L., 1992b. Non-linear temperature dependence of liquid volumes in the system albite–anorthite–diopside. *Contrib. Mineral. Petrol.* **111**, 61–73.

Knoche, R., Dingwell, D.B., Webb, S.L., 1995. Melt densities for leucogranites and granitic pegmatites: partial molar volumes for SiO_2, Al_2O_3, Na_2O, K_2O, Li_2O, Rb_2O, Cs_2O, MgO, CaO, SrO, BaO, B_2O_3, P_2O_5, F_2O_{-1}, TiO_2, Nb_2O_5, Ta_2O_5 and WO_3. *Geochim. Cosmochim. Acta* **59**, 4645–4652.

Kohara, S., Suzuya, K., Takeuchi, K., Loong, C.-K., Grimsditch, M., Weber, J.K.R., Tangeman, J.A., Key, T.S., 2004. Glass formation at the limit of insufficient network formers. *Science.* **303**, 1649–1652.

Kubicki, J.D., Lasaga, A.C., 1988. Molecular dynamics simulations of SiO_2 melt and glass: ionic and covalent models. *Am. Mineral.* **73**, 945–955.

Kubicki, J.D., Lasaga, A.C., 1991. Molecular dynamics simulations of pressure and temperature effects on $MgSiO_3$ and Mg_2SiO_4 melts and glasses. *Phys. Chem. Minerals* **17**, 661–673.

Kubo, R., 1966. The fluctuation-dissipation theorem. *Rep. Progr. Phys.* **29**, 255–284.

Lange, R.A., Carmichael, I.S.E., 1987. Densities of Na_2O–K_2O–CaO–MgO–FeO–Fe_2O_3–Al_2O_3–TiO_2–SiO_2 liquids: new measurements and derived partial molar properties. *Geochim. Cosmochim. Acta* **51**, 2931–2946.

Lange, R.A., 1996. Temperature independent thermal expansivities of sodium aluminosilicate melts between 713 and 1835 K. *Geochim. Cosmochim. Acta* **60**, 4989–4996.

Lange, R.A., 1997. A revised model for the density and thermal expansivity of Na_2O–K_2O–CaO–MgO–Al_2O_3–SiO_2 liquids from 700 to 1900 K: extension to crustal magmatic temperatures. *Contrib. Mineral. Petrol.* **130**, 1–11.

Lesher, C.E., Hervig, R.L., Tinker, D., 1996. Self diffusion of network formers (silicium and oxygen) in naturally occurring basaltic liquid. *Geochem. Cosmochim. Acta* **60**, 405–413.

Liu, Q., Lange, R.A., 2001. The partial molar volume and thermal expansivity of TiO_2 in alkali silicate melts: Systematic variation with Ti coordination. *Geochim. Cosmochim. Acta* **65**, 2379–2393.

McSween, H.Y. et al., 2004. Basaltic rocks analyzed by the Spirit rover in Gusev crater. *Science.* **305**, 842–845.

Majérus, O., Cormier, L., Calas, G., Beuneu, B., 2004. A neutron diffraction study of temperature-induced structural changes in potassium disilicate glass and melt. *Chem. Geol.* **213**, 89–102.

Marrocchi, Y., Toplis, M.J., 2005. Experimental determination of argon solubility in silicate melts: An assessment of the effects of liquid composition and temperature. *Geochim. Cosmochim. Acta* **69**, 5765–5776.

Matsui, M., 1994. A transferable interatomic potential model for crystals and melts in the system CaO–MgO–Al_2O_3–SiO_2. *Mineral. Mag.* **58A**, 571–572.

Matsui, M., 1996. Molecular dynamics simulation of structures, bulk moduli, and volume thermal expansivities of silicate liquids in the system CaO–MgO–Al_2O_3–SiO_2. *Geophys. Res. Lett.* **23**, 395–398.

Matsui, M. 1998. Computational modelling of crystals and liquids in the system Na_2O–CaO–MgO–Al_2O_3–SiO_2. Properties of Earth and planetary materials at high pressure and temperature. *Geophysical Monograph* 101 (AGU), 145–151.

Maumus, J., Bagdassarov, N., Schmeling, H., 2005. Electrical conductivity and partial melting of mafic rocks under pressure. *Geochim. Cosmochim. Acta* **69**, 4703–4718.

Melson, W.G., Thomson, G., 1971. Petrology of a transform fault zone and adjacent ridge segments. *Philos. Trans. R. Soc. Lond.* **A268**, 423–441.

Micoulaut, M., Guissani, Y., Guillot, B., 2006. Simulated structural and thermal properties of glassy and liquid germania. *Phys. Rev. E* **73**, 031504-1-11.

Mo, X., Carmichael, I.S.E., Rivers, M., Stebbins, J., 1982. The partial molar volume of Fe_2O_3 in multicomponent silicate liquids and the pressure dependence of oxygen fugacity in magmas. *Mineral. Mag.* **45**, 237–245.

Morgan, N.A., Spera, F.J., 2001. Glass transition, structural relaxation, and theories of viscosity: a molecular dynamics study of amorphous $CaAl_2Si_2O_8$. *Geochim. Cosmochim. Acta* **65**, 4029–4041.

Mungall, J.E., 2002. Empirical models relating viscosity and tracer diffusion in magmatic silicate melts. *Geochim. Cosmochim. Acta* **66**, 125–143.

Murase, T., McBirney, A.R., 1973. Properties of some common igneous rocks and their melts at high temperatures. *Geol. Soc. Am. Bull.* **84**, 3563–3592.

Mysen, B.O., 2006. The structural behaviour of ferric and ferrous ion in aluminosilicate glass near meta-aluminosilicate joins. *Geochim. Cosmochim. Acta* **70**, 2337–2353.

Mysen, B.O., Richet, P., 2005. *Silicate Glasses and Melts: Properties and Structure*. Elsevier, Amsterdam, pp. 503–520.

Navrotsky, A. 1995. *Thermodynamic Properties of Minerals. Mineral Physics and Crystallography: A Handbook of Physical Constants*, AGU Reference shelf2, pp. 18–28.

Nelson, S.A., Carmichael, I.S.E., 1979. Partial molar volumes of oxide components in silicate liquids. *Contrib. Mineral. Petrol.* **71**, 117–124.

Neuville, D.R., Courtial, D., Dingwell, D.B., Richet, P., 1993. Thermodynamic and rheological properties of rhyolite and andesite melts. *Contrib. Mineral. Petrol.* **113**, 572–581.

Neuville, D.R., Cormier, L., Massiot, D., 2004. Al environment in tectosilicate and peraluminous glasses: a ^{27}Al MQ-MAS NMR, Raman, and XANES investigation. *Geochim. Cosmochim. Acta* **68**, 5071–5079.

Nixon, P.H., Boyd, F.R. 1973. Petrogenesis of the granular and sheared ultramafic nodule suite. In: Kimberlites. Nixon, P.H. (Ed.), *Lesotho National Development*, Maseru, pp. 48–56.

Ohtani, E., Suzuki, A., Kato, T., 1998. Flotation of olivine and diamond in mantle melt at high pressure: implications for fractionation in the deep mantle and ultradeep origin of diamond. *Geophys. Mono.* **101**, 227–239.

Park, S., Ducea, M., 2003. Can in situ measurements of mantle electrical conductivity be used to infer properties of partial melts. *J. Geophys. Res.* **108** (B5), 2270.

Partzsch, G.M., Schilling, F.R., Arndt, J., 2000. The influence of partial melting on the electrical behaviour of crustal rocks: laboratory examinations, model calculations and geological interpretations. *Tectonophysics* **317**, 189–203.

Perfit, M.R., Davidson, J.P., 2000. *Encyclopedia of Volcanoes*. Academic Press, New York, pp. 89–113.

Presnall, D.C., Simmons, C.L., Porath, H., 1972. Changes in electrical conductivity of a synthetic basalt during melting. *J. Geophys. Res.* **77**, 5665–5672.

Rai, C.S., Manghnani, M.H. 1977. Electrical conductivity of basalts to 1550 °C. In: Dick, H.J.B. (Ed.), *Magma Genesis Bull.* 96, Oregon Dept. Geol. Miner. Ind., Portland, pp. 219–237.

Rai, C.S., Manghnani, M.H., 1978. Electrical conductivity of ultramafic rocks to 1820 Kelvin. *Phys. Earth Planet Int.* **17**, 6–13.

Reynolds, J.R., Langmuir, C.H., 1997. Petrological systematics of the Mid-Atlantic Ridge south of Kane: implications for ocean crust formation. *J. Geophys. Res.* **102**, 14915–14946.

Richet, P., Bottinga, Y., 1986. Thermodynamical properties of silicate glasses and liquids: a review. *Rev. Geophys.* **24**, 1–25.

Rossano, S., Ramos, A.Y., Delaye, J.-M., 2000a. Environment of ferrous iron in $CaFeSi_2O_6$ glass; contributions of EXAFS and molecular dynamics. *J. Non-Cryst. Solids* **273**, 48–52.

Rossano, S., Ramos, A., Delaye, J.-M., Creux, S., Filipponi, A., Brouder, Ch., Calas, G., 2000b. EXAFS and molecular dynamics combined study of $CaO–FeO–2SiO_2$ glass. New insight into site significant in silicate glasses. *Europhys. Lett.* **49**, 597–602.

Russel, J.K., Giordano, D., 2005. A model for silicate melt viscosity in the system $CaMgSi_2O_6–CaAl_2Si_2O_8–NaAlSi_3O_8$. *Geochim. Cosmochim. Acta* **69**, 5333–5349.

Rustad, J.R., Yuen, D.A., Spera, F.J., 1990. Molecular dynamics of liquid SiO_2 under high pressure. *Phys. Rev. A* **42**, 2081–2089.

Shibata, T., Takahasai, E., Matsuda, J-I., 1998. Solubility of neon, argon, krypton and xenon in binary and ternary silicate systems: a new view on noble gas solubility. *Geochim. Cosmochim. Acta* **62**, 1241–1253.

Shiraishi, Y., Ikeda, K., Tamura, A., Saitô, T., 1978. On the viscosity and density of the molten $FeO–SiO_2$ system. *Trans. Jap. Inst. Metal.* **19**, 264–274.

Smith, W., Greaves, G.N., Gillan, M.J., 1995. Computer simulation of sodium disilicate glass. *J. Chem. Phys.* **103**, 3091–3097.

Soules, T.F., 1979. A molecular dynamics calculation of the structure of sodium silicate glasses. *J. Chem. Phys.* **71**, 4570–4577.

Stebbins, J.F., Carmichael, I.S.E., Moret, L.K., 1984. Heat capacities and entropies of silicate liquids and glasses. *Contrib. Mineral. Petrol.* **86**, 131–148.

Stein, D.J., Spera, F.J., 1995. Molecular dynamics simulations of liquids and glasses in the system $NaAlSiO_4–SiO_2$: methodology and melt structures. *Am. Mineral.* **80**, 417–431.

Stein, D.J., Spera, F.J., 1996. Molecular dynamics simulations of liquids and glasses in the system $NaAlSiO_4–SiO_2$: physical properties and transport mechanisms. *Am. Mineral.* **81**, 284–302.

Suzuki, A., Ohtani, E., 2003. Density of peridotite melts at high pressure. *Phys. Chem. Minerals* **30**, 449–456.

Tangney, P., Scandolo, S., 2002. An ab initio parametrized interatomic force field for silica. *J. Chem. Phys.* **117**, 8898–8904.

Tinker, D., Lesher, C.E., 2001. Self diffusion of Si and O in dacitic liquid at high pressures. *Am. Mineral.* **86**, 1–13.

Tinker, D., Lesher, C.E., Hutcheon, I.D., 2002. Self diffusion of Si and O in diopside–anorthite melt at high pressures. *Geochim. Cosmochim. Acta* **67**, 133–142.

Tonks, B.T., Melosh, H.J., 1993. Magma formation due to giant impacts. *J. Geophys. Res.* **98**, 5319–5333.

Toplis, M.J., Richet, P., 2000. Equilibrium density and expansivity of silicate melts in the glass transition range. *Contrib. Mineral. Petrol.* **139**, 672–683.

Tsuneyuki, S., Tsukada, M., Aoki, H., Matsui, Y., 1988. First principles interatomic potential of silica applied to molecular dynamics. *Phys. Rev. Lett.* **61**, 869–872.

Tsuneyuki, S., Tsukada, M., Aoki, H., Matsui, Y., 1990. Molecular dynamics simulation of silica with a first-principles interatomic potential. In: Marumo, F. (Ed.), *Dynamic Processes of Material Transport and Transformation in the Earth's interior*. Elsevier, Amsterdam, pp. 1–21.

Tyburczy, J.A., Waff, H.S., 1983. Electrical conductivity of molten basalt and andesite to 25 kilobars pressure: geophysical significance and implications for charge transport and melt structure. *J. Geophys. Res.* **88**, 2413–2430.

Tyburczy, J.A., Waff, H.S., 1985. High pressure electrical conductivity in naturally occurring silicate liquids. In: Schock, R.N. (Ed.), *Point Defects in Minerals*, *Geophys. Monogr. Ser.*, 31. AGU, Washington DC, pp. 78–88.

van Beest, B.W.H., Kramer, G.J., van Santen, R.A., 1990. Force fields for silicas and aluminophosphates based on ab initio calculations. *Phys. Rev. Lett.* **64**, 1955–1958.

Vashishta, P., Kalia, R.K., Rino, J.P., Ebbsjö, I., 1990. Interaction potential for SiO_2: a molecular-dynamics study of structural correlations. *Phys. Rev. B* **41**, 12197–12209.

Vessal, B., Amini, M., Fincham, D., Catlow, C.R.A., 1989. Water-like melting behaviour of SiO_2 investigated by the molecular dynamics simulation technique. *Phylos. Mag. B* **60**, 753–775.

Vollmayr, K., Kob, W., Binder, K., 1996. Cooling-rate effects in amorphous silica: a computer-simulation study. *Phys. Rev. B* **54**, 15,808–15,827.

Waff, H.S., Weill, D.F., 1975. Electrical conductivity of magmatic liquids: effects of temperature, oxygen fugacity and composition. *Earth Planet. Sci. Lett.* **28**, 254–260.

Watson, E.B., 1994. Diffusion in volatile-bearing magmas. *Rev. Mineral. Geochem.* **30**, 371–411.

Wilding, M.C., Benmore, C.J., Tangeman, J.A., Sampath, S., 2004. Evidence of different structures in magnesium silicate liquids: coordination changes in forsterite- to enstatite-composition glasses. *Chem. Geol.* **213**, 281–291.

Woodcock, L.V., Angell, C.A., Cheeseman, P., 1976. Molecular dynamics studies of the vitreous state: simple ionic systems and silica. *J. Chem. Phys.* **65**, 1565–1577.

Wu, Z., Romano, C., Marcelli, A., Mottana, A., Cibin, G., Della Ventura, G., Giuli, G., Courtial, P., Dingwell, D.B., 1999. Evidence for Al/Si tetrahedral network in aluminosilicate glasses from Al K-edge X-ray-absorption spectroscopy. *Phys. Rev. B* **60**, 9216–9219.

Xu, Y., Shankland, T.J., Poe, B.T., 2000. Laboratory-based electrical conductivity in the Earth's mantle. *J. Geophys. Res.* **105**, 27,865–27,875.

Zhabrev, V.A., Sviridov, S.I., 2003. Ion diffusion in oxide glasses and melts: I. Bibliography. *Glass Phys. Chem.* **29**, 140–159.